Reference:
J. Song; Y. Y. Birdja; D. Pant, et al., Recent progress in the structure optimization and development of proton-conducting electrolyte materials for low-temperature solid oxide cells. International Journal of Minerals, Metallurgy and Materials 2022, 29 (4), 848-869.

ISSN 1869-103X (2022), Copyright © 2022 University of Science and Technology Beijing. All rights reserved
Full text (Publisher's DOI): https://doi.org/10.1007/s12613-022-2447-y

Received 06 November 2021; Received in revised form 14 February 2022; Accepted 28 February 2022

Recent Progress in Structure Optimization and Development of Proton-Conducting Electrolyte Materials for Low-Temperature Solid Oxide Cells

Jia Song, Yuvraj Y. Birdja, Deepak Pant, Zhiyuan Chen*, Jan Vaes*

Separation & Conversion Technology, Flemish Institute for Technological Research (VITO), Boeretang 200, Mol 2400, Belgium

Abstract

Technologies to develop low-temperature solid oxide cells (LT-SOCs) are reviewed. These technologies can be applied both in fuel cells and in electrolyzers which operates at temperatures below 500 °C, providing a more cost-effective alternative as compared to the more established high-temperature SOCs. Two routes are discussed here and show potential to reduce the operating temperature of the SOCs towards below 500 °C. On one side, as a principal way to enhance the performance of the cell, namely the structure optimization which includes reduction of electrolyte thickness to nanometer scale and exploration of electrode structure with low polarization resistance, is firstly reviewed. On the other side, the development of novel proton-conducting electrolyte materials is in the frontier of SOCs study. The fundamentals of proton conduction and design principles of the most used electrolyte materials are briefly explained. The most widely studied electrolyte materials for LT-SOCs, perovskite-type $BaCeO_3$- and $BaZrO_3$-based oxides, as well as the effect of doping on the physical-chemical properties of these oxide materials are summarized.

Keywords: Low-temperature solid oxide cells, perovskite, doping, thin-film

Content

* E-mail: zhiyuan.chen@vito.be
* E-mail: jan.vaes@vito.be

1. Introduction

A fuel cell converts chemical energy stored in fuel to electrical energy via electrochemical reactions by harvesting the Gibbs free energy of the controlled combination of fuels with oxygen on the electrodes, which generates a potential difference between the two electrodes. Similarly, an analogous cell can also be developed for water or CO_2 electrolysis. The reverse reactions are achieved when a voltage is applied to the cell, forcing a redox exchange in the electrolyzer. A reversible cell can work both in fuel cell and in electrolysis cell mode by varying the operating conditions. Major H_2 fuel cell technologies include solid oxide cells (SOCs) and proton exchange membrane cells (PEM). Traditional PEM cells work at room temperature, while SOCs usually operates at above 700 °C. Increasing the operating temperature increases the reaction kinetics therefore promises a higher energy efficiency. Meanwhile, it is generally agreed that high temperature increases the cost of key materials in the cell and detriments the durability of the cell due to the degradation of cell components. The application of high-temperature polymer electrolyte membrane (HT-PEM) can elevate the operating temperature of PEM cells to 220 °C [1].Comparatively, it is well known that the high operating temperature range of SOCs (800-1000 °C) already decreased to an intermediate temperature range of 500-800 °C. In recent papers, SOCs that operates at a temperature as low as 250 °C, although with limited performance, have been reported [2]. Such development enhances the long-term performance stability of the cells and lowers the critical requirement of material properties including the corrosion resistance of

interconnector materials, chemical compatibility of components, and stability of sealing materials. It also benefits the rapid start-up and reduces the influence of thermo-cycling in practical applications. Previous generation SOCs rely on pure oxygen-ion (O^{2-}) conductor, such as yttrium stabilized zirconia(YSZ) and gadolinium doped ceria (GDC), as electrolyte. However, the activation energy of the ionic conductivity for these electrolyte materials is found to be high (~1 eV), causing the ionic conductivity to drop to below 1 mS cm^{-1} at 600 °C. Recent developments and applications of proton-conducting electrolytes [3] and hybrid proton-oxygen conducting electrolytes [4] promote the development of low-temperature (LT-) SOCs of which the operation temperature is below 500 °C. These two types of electrolyte materials show a lower activation energy of ionic conductivity, enabling the development of the SOCs in the LT range [5]. Moreover, the exploration of new electrolytes with high protonic conductivity and active electrodes with low polarization resistance drives the operating temperature to the possibility of even low temperatures.

This work provides a review of the technologies to lower the operating temperature of SOCs with emphasis on cell structure optimization and materials design of the electrolyte. The strategies in the development of cell structures are summarized and doping is discussed as an efficient strategy to design the electrolyte material of LT-SOCs along with the evaluation of the typical proton-conducting oxide materials.

2. Development of LT-SOCs structure

The continuous efforts to optimize the structure of the cells and exploration of new materials lead to the reduction of the operation temperature of SOCs. Structure optimization has been approved as an efficient method to enhance the performance of the cell. It includes (1) producing thin-film electrolyte membranes and (2) the development of 3-D nano-structured electrodes with low polarization resistance. Especially, the fabrication of a thin-film electrolyte is a promising method to reduce the working temperature of SOCs.

2.1. Thin-film electrolyte

Reducing electrolyte thickness between electrodes lowers the ohmic resistance of the cell. During the fabrication of the thin-film ceramic electrolyte, pinholes formation is the most common issue, resulting in the cross-over of gases and subsequently in reduced cell performance. In the traditional process, a high sintering temperature of 1600 °C is generally needed for the densification of electrolyte pellets because of the poor sinterability of proton conducting ceramics. Efforts has been put into improving the sinterability of the electrolyte materials by doping and adding sintering aids [6]. Besides,

novel synthesis methods are developed to avoid high sintering temperature and to give the possibility to produce dense thin-film electrolyte in nano-meter thickness. The reported technologies include pulsed laser deposition (PLD), atomic layer deposition (ALD), sputtering, etc (Fig. 1). Among those methods, PLD is one of the most popular technologies used in lab scale experiments. It was proposed to be the best among the physical vapor deposition (PVD) technologies for ceramic film deposition[7]. PLD can realize the preparation of nanosized porous film and dense film [8-11].It also optimizes the crystal structure of the film to reduce the ohmic resistance of the electrolyte. The ohmic resistance of a PLD fabircated yttrium-doped barium zirconate membrane was reduced to 0.2 $\Omega \cdot cm^2$ at 450 °C by constructing a grain-boundary-free columnar strcture [12]. However, lacking of upscaling capability limits the application of PLD for practical implementation.

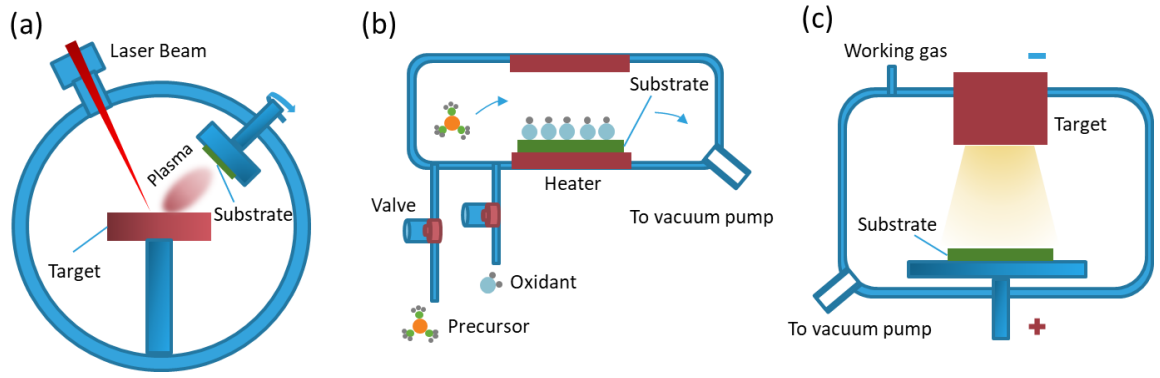

Fig. 1 Schematic representations of (a) PLD; (b) ALD; (c) Sputtering system.

ALD has the capability to deposit conformal films in several atomic layers to nanometer thickness on materials with either flat or tortuous surfaces. It is an efficient approach to prepare high-quality nano-scale electrolyte thin films and improve the durability of the nano-structure electrode of SOCs [13]. However, the formation of a dense and continuous electrolyte film needs a matrix which is either a smooth and dense substrate such as another electrolyte film [14, 15], or a porous matrix with small pore sizes at one side, where the diameter of the pore should be smaller than the thickness of the ALD coating film. Moreover, the electrolyte will be deposited in the internal pores of the matrix and reduce the pore size during the process [16]. That means that the porosity and surface chemical composition of the matrix will be changed by ALD. Therefore, the application of ALD for thin-film electrolyte preparation is usually limited to silicon wafers. Baek *et al*. [17] reported an ALD-etching-ALD process to produce a 10 nm thick electrolyte with high performance. A patching layer with small electrolyte grains fixes the sub-layer with large electrolyte grains in the film and contributes a high density of grain boundaries within the film. The mechanical properties of the film are therefore enhanced, so

that it can be thin enough to reach the lower limit of electrolyte thickness (6 nm for yttria-stabilized zirconia) [18] and still retain high performance.

Sputtering was practiced for the deposition of electrolytes on silicon wafers[19], porous anodic aluminium oxide (AAO) substrates [15], and ceramic electrode substrates [20]. Moreover, it was also used for the coating of electrodes on the thin-film membrane [17]. Some studies employed suspension spray coating [21], which is a facile and economical technology compared to the aforementioned vacuum deposition methods. The challenge of spray coating is that it has a high potential to introduce a more porous microstructure compared to PLD and the other PVD technologies. Therefore, parameters for the spraying process need to be well controlled to optimize the microstructure of the membrane. Electrostatic spray deposition (ESD) technology has been applied for spray pyrolysis of electrolyte membrane since the 1990s [22-24]. The droplets created during the electrospraying process can be controlled to a few nanometer due to their interaction with the electric field. The thickness of the deposited film can be precisely controlled because the electrostatic forces disperse the nanoscale droplets homogeneously over the substrate. More importantly, it is possible to fabricate a thin layer with various surface morphology and microstructure by adjusting the process parameters [25, 26]. Notably, there are alternative methods to fabricate large-area dense thin-film electrolyte, such as physical vapor deposition (PVD), electrophoretic deposition (EPD), and chemical solution deposition (CSD) [27-30]. Fig. 1 illustrates three methods, i.e. PLD, ALD and sputtering, that have been adopted in recent studies to fabricate thin dense electrolyte membranes.

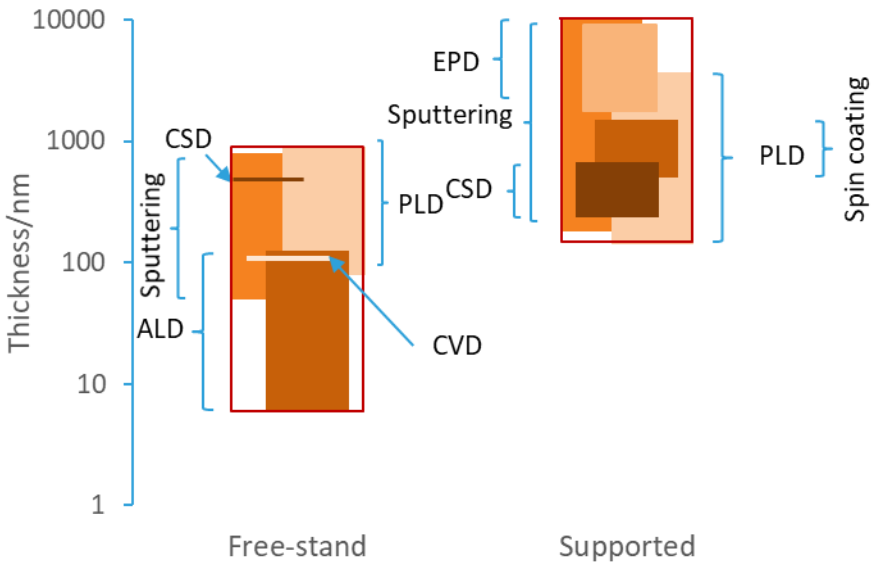

Fig. 2 Thickness of free-standing and supported electrolyte membranes which were fabricated with different methods in the recent reports [7-9, 17, 20, 21, 28-36].

As shown in Fig. 2, two types of thin-film electrolytes, i.e. free-standing electrolyte and supported electrolyte, can be prepared by the aforementioned coating technologies. Free-standing electrolyte membrane is usually deposited on a silicon wafer, after which a layer of electrode will be deposited on top of the electrolyte layer. Limited by the mechanical properties of the membrane, the thickness of the free-standing electrolyte is usually in tens of micrometers. To reduce the risk of potential mechanical failure, Baek *et al*. [17] suggested to reduce the lateral dimension of the membrane and to refine the grains. Meanwhile, they proposed that a dish-shape window rather than a square could improve the mechanical stability of the free-standing membrane (Fig. 3). Other than that, researchers have developed several complex structures, e.g. V-cup-shape structure, to improve the quality and performance of the thin-film [37, 38].

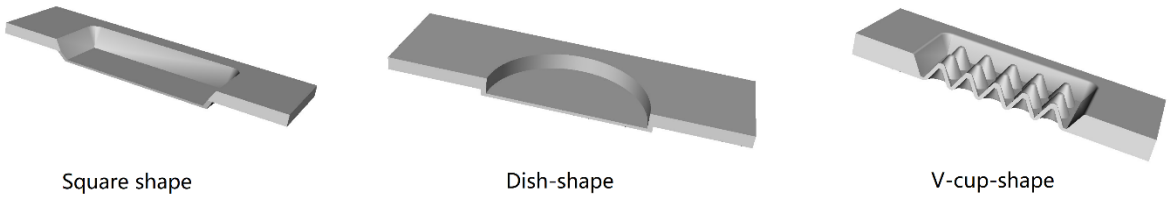

Fig. 3 Shape of free-stand membranes

The free-standing electrolyte is sensitive to its complex fabrication process, which makes it difficult to scale up at a low cost [34, 39]. As a result, the limited practicality and high manufacturing cost of SOCs with free-standing electrolyte hinder the success of its commercial application. A supported electrolyte configuration uses a porous matrix as the base for the thin-film electrolyte to growth on. This approach yields a better resistance to potential thermal shocks of supported electrolyte compared to that of the free-standing electrolyte. If the porous electrode is designed as the substrate, the reaction interface area can be extended from 2D to 3D structure by introducing high density triple-phase boundary into the electrode, which promotes reaction kinetics. The developments of the porous matrix, aimed at increasing the reactive surface area of the cells and at improving its thermal-mechanical stability, finally leading to stable electrochemical performance during operation.

One of the challenges for the fabrication of nano-scale thin-film electrolyte is to meet the strict structural requirements of the porous matrix, that serves as the electrodes support. For instance, the waviness of the porous matrix surface needs to be controlled in a sub-μm level to prevent the defects of the coated electrolyte film [30]. High quality of the surface topography, particle size, and pore structure of the porous electrode is necessary for the successful synthesis of a nano-scale thin-film

electrolyte over the support [40]. In order to achieve this, two strategies have been proposed up to now.

In the first case, a functional layer is deposited on the surface of the original porous base layer, working as a bilayer matrix [41, 42]. Fig. 4 shows the structure configuration of a cell with functional layers. The support layer can be synthesized in a conventional process. In fact, a support layer fabricated using powders with submicron particle size distribution is beneficial for the durability of the cell [32]. The functional layer is an interlayer between the thick cathode matrix layer and the electrolyte, which should fulfil the following requirements: (1) It should be as thin as possible (from 1 to 10 µm in most cases). This thickness is desired to reduce the mass transfer resistance of the gasses, and to extend the triple-phase boundary. (2) The particle size and the pore size in the functional layer should be at least in the same range of the thickness of the thin-film electrolyte, so that a thin electrolyte layer can be successfully deposited on top of it[43, 44]. Park *et al*. [31] compared the performance of cells manufactured with and without the functional layer, their results show that the presence of a functional layer greatly promotes the performance of the cell in the low-temperature range. More importantly, they found that the functional layer with micrometer-level particles and pore sizes shows inferior enhancement to the cell performance than that with nanosized particles and pores. Furthermore, researchers developed functional layers with multilayers [12] or gradients [33], within which the porosity and a specific weight ratio between electrolyte and Ni are featured. The multilayers overlay a nano-layer on the micro-layer. They have been proven to have a positive influence on the quality of the deposited film.

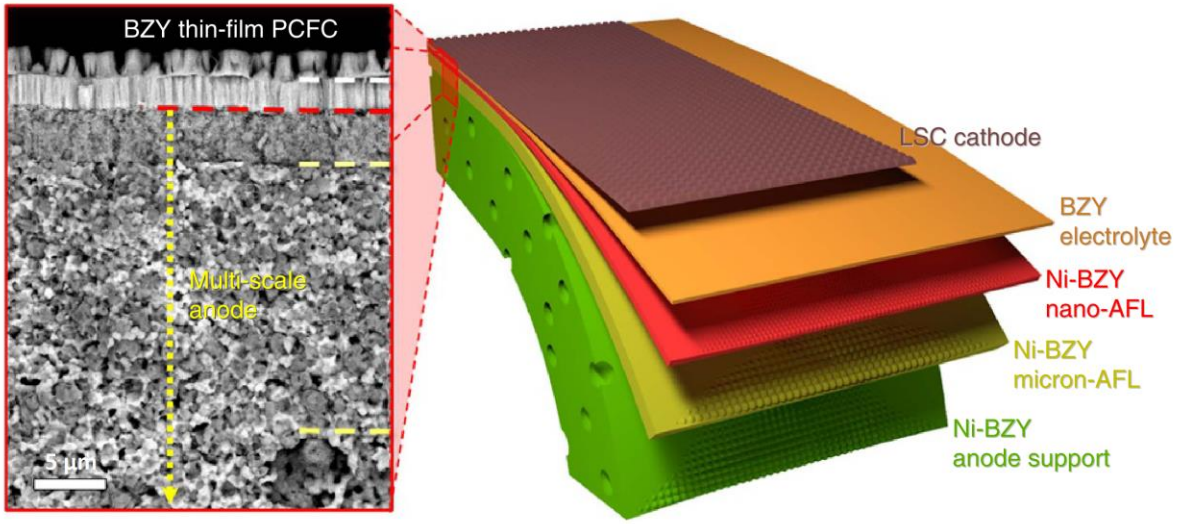

Fig. 4 Structure configuration of the fuel cell with yttrium-doped barium zirconate (BZY)/Nickel functional layers. Reprinted with permission from [12]

The other strategy is to firstly produce a homogeneous substrate layer on which a thin electrolyte layer is deposited. The substrate layer, which functions as electrode, is made of a mixture of NiO and Fe_3O_4. [45] After the assembly of the electrolyte membrane and electrode, the electrode matrix undergoes a reduction step, converting the dense ceramic to a porous cermet, thus creating the porosity that is needed for the operation of the cell.

Furthermore, the challenge of developing the solid oxide electrolysis cells (SOECs) is somewhat different from that of SOFCs because of the presence of high-partial-pressure steam that accelerates material degradation [46]. Experimental investigation of LT-SOECs is still very rare. Wang *et al*. [47] reported a reversible solid oxide cell working at 450-600 °C. A durability test at 500 °C showed a rapid degradation due to the sintering behaviour of the electrode particles. Son *et al*., who worked extensively on LT-SOFC, also reported LT-SOEC testing with different novel fuel electrode configurations, and proved a positive effect of catalyst insertion by multi-layer film PLD deposition [48]. Both works implied a need for further experimental work to overcome the negative effect of steam on electrolysis cells.

2.2. Exploration of electrode structures

The architecture of the electrode significantly influences the performance of LT-SOCs [34]. In a recent paper, Shimada *et al*. reported a SOEC system that operates at a current density of 4 A/cm^2 at 800 °C by applying a bimodal structure of nanocomposite electrodes [49]. Ding *et al*. [3] developed a nanofiber-structured steam electrode mesh which enhanced the electrochemical performance of the SOECs in the range 400 – 600 °C. Especially, a current density of 0.35 A/cm^2 was recorded at 400 °C.

The optimization of electrode architecture is related to several aspects, i.e., the annealing procedure, design of the porous structure, and cermet composition distribution. Annealing is a crucial step during the manufacturing of the electrode layer. A high annealing temperature of electrodes is needed, leading to a high energy consumption [50]. Additional issues in product quality control may arise because of the possible thermomechanical/chemical incompatibility of different components and poor phase stability of cell materials. Some of these issues could be overcome by constructing symmetrical cells [51], building interlayers [52], or carefully altering the heat treatment procedure [53, 54]. Alternatively, methods which do not involve sintering., such as depositing electrodes with sputtering [55-57], PLD [40, 58], and ALD [59], can be used to avoid the issues. Here the application of ALD to the electrode materials is to modify the catalyst surface and provides an non-sintering method to deposit electrode layer while increasing the catalytic activity of the electrode [60].

Other than optimizing he annealing procedure, efforts have been put on designing novel porous structure and architecture of the electrodes to minimize the polarization loss. The construction of nano-structured or nano-sized electrodes increases the surface areas of electrocatalytically active materials. Recently, near-one-dimensional nanofibers have been fabricated and used as the electrode of SOCs (Fig. 5). The high porosity, good interconnectivity, and continuous pathway for charged species (electrons and protons) through the three-dimensional fiber network resulted in a high-performance of the cells [61, 62]. Nanowire structures applied in Li-S batteries deliver similar intrinsic advantages; displaying potential for high active material loading and expedited highways for electron transfer and mass diffusion [63]. Utilizing such fibrous network structure as electrode was also proved to be effective in achieving quick mass transport and high electrocatalytical activity in high temperature PEM [64]. It was also reported that the application of a nano-structured 3-D network as the skeleton of the electrode can promote the performance of the SOCs [65-70].

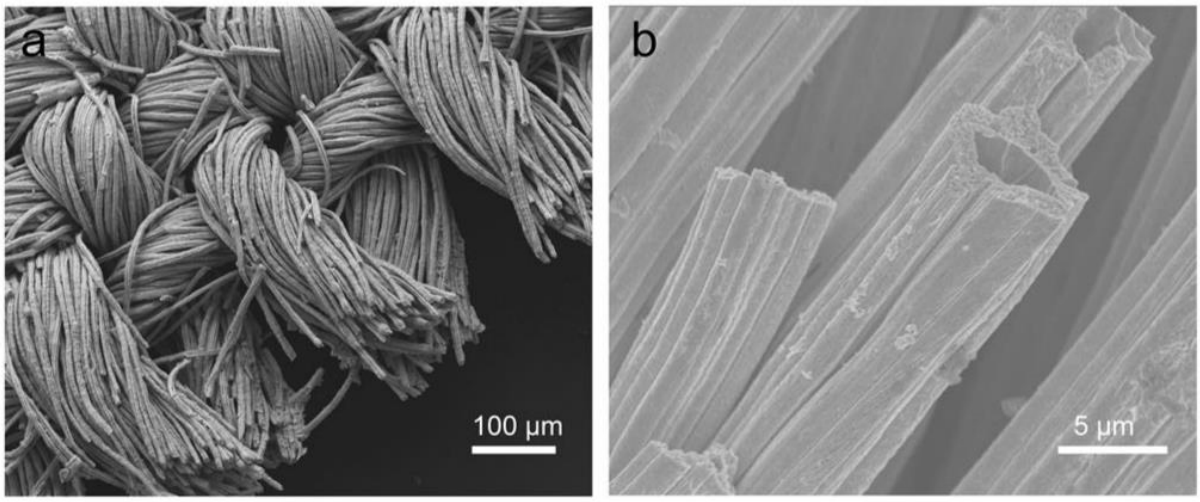

Fig. 5 Nanofiber-structured $PrNi_{0.5}Co_{0.5}O_{3-\delta}$ mesh as electrode of SOC. Each single fiber is composed of nanoparticles with diameter ranging from 20 to 50 nm. Reprinted with permission from [3]

The introduction of electrocatalytically active nanoparticles into the 3-D network of the electrode has been reported to improve electrochemical performance for oxide cells. Methods to achieve it include infiltration [71], precipitation [72], and deposition [73]. However, the introduction of nanoparticles on the electrode surfaces struggles with non-uniform size and composition of the particle, leading to sub-optimal performance. Furthermore, the uneven distribution of the catalysts in the electrode might result in the suppressed performance of the electrode. The in-situ exsolution was developed as a promising method to manufacture nanoparticle-decorated electrodes (Fig. 6). Up to now, only conventional perovskite oxides have served as substrates for in-situ growth of the metal nanoparticles.

Thus, the exsolution of nanoparticles could be limited by energetic barriers toward removing B-site cations from a stoichiometric perovskite [74].

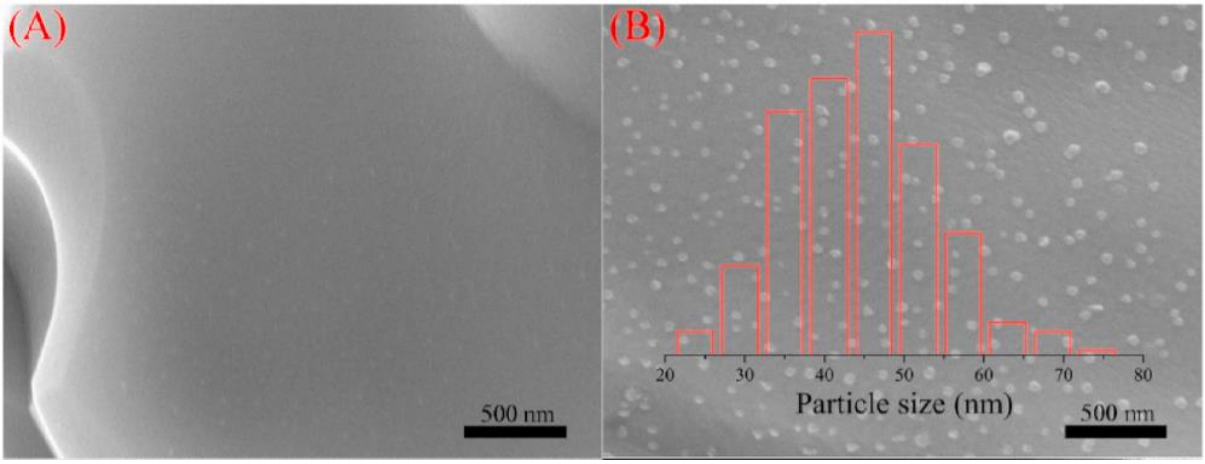

Fig. 6 SEM images of the $La_{0.7}Sr_{0.3}Fe_{0.9}Ni_{0.1}O_{3-\delta}$ backbone (a) before and (b) after the in-situ exsolution Ni-Fe alloy nanoparticles. Reprinted with permission from [75]

The optimization of the composition distribution include not only dispersing particles in the porous electrode matrix, but also depositing a thin-film coating on the electrode [76]. It has been reported that the stability and electro-catalytic activity can be enhanced by thin-film coating on the skeleton of the electrode. Further, the polarization resistance of the commonly used Pt cathode was lowered by ZrO_2 capping. This enhancement was attributed to the discontinuous ZrO_2 film facilitating oxygen adsorption on the cathode surface and decreasing the oxygen adsorption-desorption resistance [77]. The catalysis enhancement of Pt by a highly uniform nano scaled YSZ overcoating has been discussed in the literature. The YSZ overcoat on Pt can be suggested as a significant facilitator of chemical processes related to atomic species during electrochemical catalysis [78, 79].

As stated above, optimization of the cell structure is one of the efficient ways to promote the performance of SOCs. The other way is to develop noble materials which show better intrinsic properties at low temperature range.

3. Proton-conducting electrolyte materials for LT-SOCs

The electrolyte layer serves as an electronic insulator to separate the cathode and anode while allowing the ions to pass to keep the current flowing through the external circuit and maintain the charge balance. The materials for the electrolyte of the SOEC must fulfil the following requirements:

a. Sufficient ionic conductivity and negligible electronic conductivity at the operating condition.

b. Exceptional chemical stability in both reducing and oxidizing atmospheres to which the electrolyte layer is exposed.
c. Physical and chemical compatibility with common electrode materials such as the perovskite-oxide air electrode and Ni-cement steam electrode.
d. Acceptable sinterability of the material to ensure the gas tightness of the electrolyte layer.

To date, materials with fluorite, perovskite, and related structures have been considered as electrolyte materials for SOEC. These materials can be categorized as either oxygen anion or proton conductors. The conduction of protons generally has lower activation energy (E_a) than the conduction of oxygen ions. Hence, the application of the proton conductors, in comparison with the oxygen conductors, effectively lowers the operating temperature of the LT-SOEC from 400 – 600 °C to 250 – 550 °C. Fig. 7 shows the temperature dependence of the proton conductivity of the most important pure proton conductors.

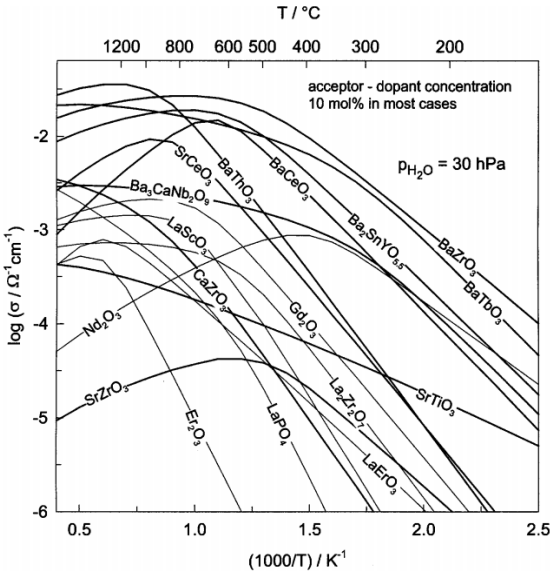

Fig. 7 Proton conductivity of the most important LT-SOCs electrolyte materials as a function of inverse temperature. Some data were calculated from available data on proton concentrations and mobilities for an extended temperature range, for which conductivities are not always accessible experimentally. Reprinted with permission from [80].

The proton conductors were introduced for SOCs in the 1980s by Iwahara *et al*.[81-84] Of these materials, the perovskite-type ceriates and zirconia, e.g., $BaCeO_3$ and $BaZrO_3$-based materials, have remained benchmark materials for high proton conductivity in oxides.[85] Since then, various materials based on these compositions have been synthesized aiming to improve their performance in SOCs. Although many other oxides have also been investigated, we do not intend to cover a wide range of materials in this article, as other excellent reviews are available.[80, 86-90]

To effectively improve the perovskite oxides, it is important to understand the mechanism of proton conduction in these materials.

3.1. Fundamentals of the proton conductivity in the perovskite oxides

Both $BaCeO_3$ and $BaZrO_3$ are $A^{2+}B^{4+}O_3$ type perovskites, where A and B are two types of cations. The B-site cations are six-fold coordinated with oxygen atoms to form corner sharing BO_6 octahedra, while A cations occupy the voids created by the octahedra. Protons in the perovskites reside as a hydroxide anion on a site of an oxygen ion, as $\mathrm{OH}_{\mathrm{O}}^{\bullet}$ in Kröger-Vink notation. The conductivity of proton is thermally-activated and described by an Arrhenius dependence (Eq. 1),

$$\sigma_{\mathrm{OH}_{\mathrm{O}}^{\bullet}} = \sigma_{\mathrm{OH}_{\mathrm{O}}^{\bullet}}^{*} \exp\left(-\frac{E_{\mathrm{a}}}{kT}\right) \quad (1)$$

Where, E_a is the activation energy for proton conduction, k the Boltzmann constant, and T the temperature, the pre-exponential Factor $\sigma_{\mathrm{OH}_{\mathrm{O}}^{\bullet}}^{*}$

can be expressed as,

$$\sigma_{\mathrm{OH}_{\mathrm{O}}^{\bullet}} = -\frac{z_{\mathrm{OH}_{\mathrm{O}}^{\bullet}} F [\mathrm{OH}_{\mathrm{O}}^{\bullet}] \mu_{\mathrm{OH}_{\mathrm{O}}^{\bullet}}}{V_{\mathrm{M}}} \quad (2)$$

Where, $z_{\mathrm{OH}_{\mathrm{O}}^{\bullet}}$ is the charge of the proton, F the Faraday constant, $[\mathrm{OH}_{\mathrm{O}}^{\bullet}]$ the proton concentration in the oxide, $\mu_{\mathrm{OH}_{\mathrm{O}}^{\bullet}}$ the proton mobility, and V_M the molar volume of the perovskite oxide. Therefore, proton conductivity is essentially dependent on the proton concentration and proton mobility. For the material to effectively conduct ions, a humid environment is needed.

3.1.1. Hydration

The formation of the proton defects in the perovskites at moderate temperature, which is usually referred to as the hydration process, relies on oxygen vacancies ($\mathrm{V}_{\mathrm{O}}^{\bullet\bullet}$). The oxygen vacancies in $A^{2+}B^{4+}O_3$ type perovskites are usually created by doping the B-site cations with a trivalent element M (acceptor dopant). The defect equation (Eq. 3), in Kröger-Vink notation, shows the process:

$$\mathrm{M}_2\mathrm{O}_3 \rightarrow 2\mathrm{M}_{\mathrm{B}}' + 3\mathrm{O}_{\mathrm{O}}^{x} + \mathrm{V}_{\mathrm{O}}^{\bullet\bullet} \quad (3)$$

The reaction that leads to the proton defect formation starts from the dissociative absorption of H_2O into a hydroxide ion and proton, followed by the incorporation of the hydroxide ion into the oxygen vacancy and formation of a covalence bond between a proton with lattice oxygen, thus creating two hydroxyl substituents:

$$H_2O + V_O^{\bullet\bullet} + O_O^x \leftrightarrow 2OH_O^{\bullet} \quad (4)$$

During the hydration reaction of acceptor-doped perovskite oxides, three key factors are involved; the formation energy of oxygen vacancies, the hydration energy and the local structural configuration of the dopants, oxygen vacancies, and protons. [91]

The thermodynamics of the hydration reaction can be experimentally evaluated from the proton concentration of the materials as a function of temperature.[92] In a controlled atmosphere, the concentration of the proton defect is determined by the equilibrium constant of the hydration reaction (K_{hyd}),

$$K_{\mathrm{hyd}} = \frac{[OH_O^{\bullet}]^2}{p_{H_2O}[V_O^{\bullet\bullet}][O_O^x]} \quad (5)$$

K_{hyd} can be related to the Gibbs free energy (ΔG_{hyd}), enthalpy (ΔH_{hyd}), and entropy (ΔS_{hyd}) of the hydration reaction by the Van 't Hoff equation (Eq. 6) as,

$$\Delta G_{\mathrm{hyd}} = -RT\ln K_{\mathrm{hyd}} = \Delta H_{\mathrm{hyd}} - T\Delta S_{\mathrm{hyd}} \quad (6)$$

$$\ln K_{\mathrm{hyd}} = -\frac{\Delta H_{\mathrm{hyd}}}{RT} + \frac{\Delta S_{\mathrm{hyd}}}{R} \quad (7)$$

Therefore, the hydration reaction is favored with a more exothermic ΔH_{hyd}, a less negative ΔS_{hyd}.

The energetic impact of local structure configuration of the proton, oxygen vacancies, and acceptor dopants on the hydration reaction is rather complicated. A recent density functional theory (DFT) study suggested that the hydration energy varies significantly with the local defect structures. [91] There are two main configurations of local defects depending on the interaction between acceptor dopants and oxygen vacancy, i.e. (a) associated M-V_O-M configuration and (b) isolated configuration, as shown in Fig. 8. The isolation of the defects is mostly found to decrease the hydration energy, which is beneficial to the hydration process.

Next to the amount of protons in the material, , we'll need to discuss their mobility in the material to understand the resulting proton conductivity.

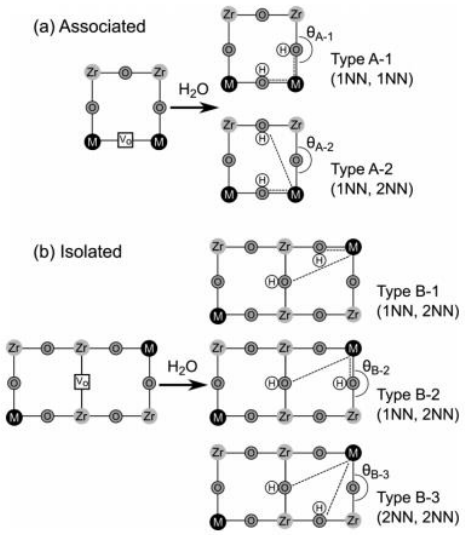

Fig. 8 Schematic representation of the hydration process by the reaction of H_2O molecule. (a) Associated (type A) and (b) isolated (type B) configurations of complex defects ($2M'_{Zr}$, $V_O^{\bullet\bullet}$) before hydration. 1NN and 2NN denote H atom site at the first and second nearest neighbor from dopant M, respectively. Reprinted with permission from [91].

3.1.2. Proton diffusion

The diffusion of a proton, which resides on a host oxygen ion, is commonly interpreted based on the Grotthuss mechanism: (1) inwards thermal rotational motion of the OH-B-O bonds to create distance minima between two O atoms and (2) proton hopping between two adjacent O atoms due to stretching vibrations of the hydrogen bond. Jing *et al*.[93] illustrated the migration pathway of the proton by performing detailed DFT calculations, as shown in Fig. 9 below.

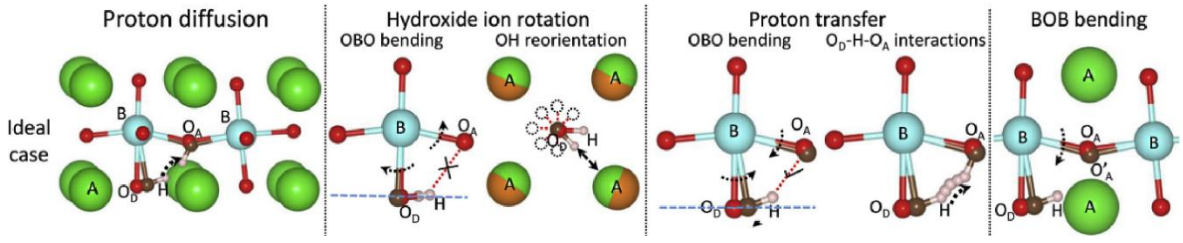

Fig. 9 Schematic illustration of the proton diffusion mechanism in an ABO_3 perovskite oxide. The left figure shows the proton diffusion mechanism in 3D structures: hydroxide ion rotation in the AO plane and proton transfer in BO_2 plane. Middle two figures describe the elementary steps underlying hydroxide ion rotation: outward O-B-O bending motion and hydroxide ion reorientation in AO plane,

and proton transfer: inward O-B-O bending motion, hydroxide ion rotation out of AO plane, and O_D-H-O_A interactions in BO_2 plane. The right figure shows additional B-O-B bending motion involved in both hydroxide ion rotation and proton transfer. The red balls denote the initial positions, and the brown balls show the final positions. Reprinted with permission from [93]

Owing to the nature of the Grotthuss mechanism, a proton must overcome two energy barriers during the migration; the activation energies for the hydroxide ion to rotate and for the proton to jump. They depend significantly on the local chemical and defect environment, A or B site ion, dopant, and oxygen vacancies. When trivalent dopants (M) are used to create oxygen vacancies, the negatively charged M_B' defect attracts protons, hindering its further migration. Such proton-dopant association is called proton trapping. Generally, the smaller the dopant ion is, the more densely charged it is, leading to greater attraction between the dopant and proton.[94-99] Since oxygen vacancies is also imply a positive charge, they tend to be located around the dopant, forming $V_O^{\bullet\bullet} - M_B'$ clusters. Remarkably, the proton trapping near dopants can be alleviated due to the repulsion between protons and $V_O^{\bullet\bullet} - M_B'$ clusters, since both have a net positive charge.[100, 101]

3.2. Effect of doping on the performance of $BaZrO_3$- and $BaCeO_3$-based proton-conducting electrolyte

As mentioned before, perovskite-type $BaCeO_3$- and $BaZrO_3$-based oxides are the most widely studied electrolyte materials for LT-SOEC. In general, $BaCeO_3$ shows high proton conductivity due to the relatively large ionic radius of Ce. The large Ba and Ce ions create large lattice free volume in the perovskite lattice, which favours proton migration. For instance, Wang *et al*. found the total ionic conductivity in $BaCe_{0.8}Y_{0.15}Nd_{0.05}O_3$ to be 8.16 mS cm^{-1} in a wet hydrogen atmosphere at 500 °C.[102] However, Ce-rich compositions suffer from low chemical stability under H_2O and CO_2 containing atmosphere due to the following reactions:[103-105]

$$BaCeO_3 + H_2O \rightarrow Ba(OH)_2 + CeO_2 \quad (8)$$

$$BaCeO_3 + CO_2 \rightarrow BaCO_3 + CeO_2 \quad (9)$$

Hence, the focus of ongoing studies on $BaCeO_3$-based materials is to improve the chemical stability while preserving the high proton conductivity of the material.

In comparison, $BaZrO_3$ shows excellent chemical stability under humid and CO_2-rich atmospheres, and high bulk proton conductivity (0.024 S cm^{-1} at 400 °C) [106] below 600 °C. Kim *et al*. demonstrated that $BaZr_{0.85}Y_{0.15}O_3$ has excellent chemical stability in 100% CO_2 over the temperature range of 25 – 1450 °C, while preserving adequate resistance to water.[104] However, the sintering temperature of

the $BaZr_xY_zO_3$ is prohibitively high, (e.g., 1600 °C for $BaZr_{0.8}Y_{0.2}O_3$.[107]) Furthermore, the total proton conductivity of the polycrystalline $BaZrO_3$ is often hindered by grain boundary blocking effects due to significantly lower proton conductivity at the grain boundary than that in the bulk.[108, 109]

Because both $BaCeO_3$ and $BaZrO_3$, are easily formed solid solutions, numerous studies have been conducted to mix $BaCeO_3$ and $BaZrO_3$ to reach optimal compromises between the good proton conductivity of $BaCeO_3$ and excellent chemical stability of $BaZrO_3$.[110, 111] Although not completely stabilized, the $BaCe_{1-x}Zr_xO_3$ system shows improved resistance compared to $BaCeO_3$ system.[112, 113]

Among the large number of studies to optimize the performance of the proton conducting materials, the most effective means seem to be doping and applying sintering aids. The most common strategy to improve the performance of $BaCeO_3$ and $BaZrO_3$ materials as electrolyte materials was doping the B-site of the perovskite oxides with trivalent elements. The commonly used elements include Sc, Y, In, Pr, Nd, Sm, Gd, Er, and Yb. Depending on the dopant ion and doping concentration, multiple properties such as proton conductivity, chemical stability, sinterability are heavily influenced.

3.2.1. Proton conductivity

As elucidated above, acceptor type dopants create the oxygen vacancies which are vital for hydration. The influence of dopant types and concentration on the formation of oxygen vacancies and on the hydration energy have been assessed experimentally and theoretically. However, no correlation between the dopant ion and the formation energy of oxygen vacancy has been found. For instance, Takahashi *et al*. calculated the formation energy of oxygen vacancy of 3.1 % acceptor-doped (Al, Sc, Ga, Y, In and Lu) $BaZrO_3$ using DFT calculations.[91] The calculated energy follows the trend Al < Ga < Y < In < Lu < Sc, as Sc doped $BaZrO_3$ is the most difficult composition to form oxygen vacancy. Meanwhile, Bévillon *et al*. found that when the dopant level is 25% , the formation energy follows a similar order: Ga < In < Y < Sc.[114] He *et al*. also noticed that the effects of Nd and Y dopants on the formation energy of oxygen vacancies in $BaZrO_3$ are opposite to those in $BaCeO_3$.[115] On the other hand, the formation enthalpy of oxygen vacancy was suspected to become more exothermic with increasing dopant concentration. For instance, Gonçalves *et al*. found that the formation enthalpy of oxygen vacancy in the $BaZr_{1-x}Y_xO_3$ system gradually changed from -49.11 kJ mol^{-1} for x = 0 sample to -126.97 kJ mol^{-1} for x = 0.5 sample using drop solution calorimetry.[116]

Table 1 Hydration enthalpy and entropy for typical doped $BaZrO_3$-, $BaCeO_3$-, and $BaCe_{1-x}Zr_xO_3$-based electrolyte materials reported in the literature.

The hydration enthalpy and entropy for doped $BaZrO_3$ and $BaCeO_3$ systems can be experimentally obtained by fitting the water uptake data measured by thermogravimetry (TG) to Eq. 7. Table 1 summarizes these values for typical doped $BaZrO_3$-, $BaCeO_3$-, and $BaCe_{1-x}Zr_xO_3$- electrolyte materials. While differences in the reported values of the hydration enthalpy and entropy were found for the same composition, certain consistency can also be observed. For instance, the reported hydration enthalpies for $BaZr_{0.8}Y_{0.2}O_3$ and $BaZr_{0.9}Y_{0.1}O_3$ are generally around 93 kJ mol^{-1} and -80 kJ mol^{-1}, respectively. However, a different enthalpy value of -22 kJ mol^{-1} for $BaZr_{0.8}Y_{0.2}O_3$ has also been reported. Such discrepancy is likely due to the limited data quality of equilibrium measurements, e.g. TG, conductivities, etc.. Overall, the hydration enthalpies of barium cerates are more negative than those of barium zirconates, suggesting a better hydration ability of barium cerates. The impact of dopant to the hydration can be evaluated using the weighted Allred-Rochow electronegativities for the occupants of the B and A site ($\Delta X_{B\text{-}A}$), i.e., small B-A electronegativity differences have more negative hydration enthalpies. According to Table 2, the $\Delta X_{B\text{-}A}$ of the $BaCeO_3$- and $BaZrO_3$-based proton conductors follow the trend of Yb < Ce < Y = Gd = Er < Sc < Zr < In. Such trend is generally reflected in the data of hydration enthalpy of doped $BaCeO_3$- and $BaZrO_3$-based proton conductors as shown in Table 1.

Table 2 Allred-Rochow electronegativities (χ^{AR}) of A, B site elements and the weighted Allred-Rochow electronegativities for the occupants of the B and A sites of the selected proton conducting perovskites.

Elements	Ba	Zr	Ce	Y	Sc	In	Gd	Yb	Er
χ^{AR}	0.97	1.22	1.08	1.11	1.20	1.49	1.11	1.06	1.11
$\Delta X_{B\text{-}A}$	-	0.25	0.11	0.14	0.23	0.52	0.14	0.09	0.14

The influence of dopants on proton diffusion has widely been studied. The two most-used parameters to evaluate proton diffusion are the proton diffusion coefficient and the energy barrier (activation energy) for proton conductivity. With a higher proton diffusion coefficient, the proton diffuses faster through the oxides. Meanwhile, the energy barrier for proton diffusion, which is a thermally-activated process, gives an indication about the difficulty of proton migration in the proton conductor. Generally, the lower the proton migration energy barriers are, the better the proton conductor performs at a relatively low temperature. The migration energy barrier obtained experimentally and theoretically are listed in Table 3.

Table 3 Calculated energy barrier for proton migration of acceptor doped barium zirconates and cerates reported in the literature.

Materials	Method	Temperature range (°C)	p_{H_2O} (atm)	E_a (eV)	Ref.
$BaZr_{0.9}Sc_{0.1}O_3$	Conductivity + TG	90-200	0.023	0.5	[117]
$BaZr_{0.9}In_{0.1}O_3$	Conductivity + TG	80-325	0.023	0.48	[117]
$BaZr_{0.98}Y_{0.02}O_3$	Conductivity + TG	90-325	0.023	0.44	[117]
$BaZr_{0.95}Y_{0.05}O_3$	Conductivity + TG	70-290	0.023	0.44	[117]
$BaZr_{0.9}Y_{0.1}O_3$	Conductivity + TG	40-150	0.023	0.43	[117]
$BaZr_{0.9}Y_{0.1}O_3$	Conductivity + TG	50-300	0.04	0.44	[127]
$BaZr_{0.8}Y_{0.2}O_3$	Conductivity + TG	50-150	0.023	0.48	[117]
$BaZr_{0.9}Gd_{0.1}O_3$	Conductivity + TG	30-110	0.023	0.47	[117]
$BaCe_{0.98}Y_{0.02}O_3$	Conductivity + TG	50-275	0.023	0.48	[117]
$BaCe_{0.95}Y_{0.05}O_3$	Conductivity + TG	50-200	0.023	0.50	[117]
$BaCe_{0.9}Y_{0.1}O_3$	Conductivity + TG	50-225	0.023	0.54	[117]
$BaCe_{0.85}Y_{0.15}O_3$	Conductivity + TG	80-250	0.023	0.60	[117]
$BaCe_{0.8}Y_{0.2}O_3$	Conductivity + TG	125-200	0.023	0.63	[117]
$BaZr_{0.875}Ga_{0.125}O_3$	DFT	-	-	0.62	[128]
$BaZr_{0.875}Sc_{0.125}O_3$	DFT	-	-	0.49	[128]
$BaZr_{0.875}In_{0.125}O_3$	DFT	-	-	0.36	[128]
$BaZr_{0.875}Y_{0.125}O_3$	DFT	-	-	0.3	[128]
$BaZr_{0.875}Gd_{0.125}O_3$	DFT	-	-	0.33	[128]
$BaZr_{0.875}Y_{0.125}O_3$	Quantum mechanics calculation	-	-	0.41	[129]

As discussed above, the proton trapping show a negative correlation with the dopant radius. Stocks and Islam calculated the dopant-OH binding energy as a function of the dopant size and found that the binding energy decreased with increasing ion size of dopants, from -0.8 eV for Sc (0.745 Å) to -0.3 eV for Y (0.900 Å).[94] Using DFT, Björketun *et al*. calculated the activation energy of proton migration in a 12.5% M doped $BaZrO_3$ system (M = Ga, Sc, In, Y, and Gd). They found that the theoretical proton migration energy in the $BaZr_{0.875}M_{0.125}O_3$ system follows the order of Ga > Sc > In > Gd > Y.[128] Together with other DFT calculations [124, 130, 131], this supports the claim that larger ions reduce proton trapping.

Additionally, the dopant concentration influences the local distortion of the lattice and the oxygen vacancy concentration. A recent DFT-study DFT suggested an overall positive correlation between local oxygen distortion and proton trapping. They found the dopant-proton interaction energy becomes more favorable when a lower level of local distortion is present, i.e., a lower concentration of dopants.[132]

The experimental activation energy for proton migration can be extracted from the oxygen bound proton diffusion coefficient ($D_{\sigma_{OH_O^\bullet}}$). By combining the data of total conductivity and proton concentration, determined from TG measurements, the diffusion coefficient is obtained via the Nernst-Einstein relationship. The activation energies calculated from the diffusion coefficient are

included in Table 3. The dependence of the experimental activation energies with the dopant ion sizes is in agreement with the theoretical ones. The Arrhenius plot of the proton diffusion coefficients of several $BaZrO_3$- and $BaCeO_3$-based proton conductors are summarized in Fig. 10. The yttrium dopants seem to have a detrimental effect on the diffusion of proton in the barium cerates, while an opposite effect was observed in the barium zirconates. In the measured temperature range, the Ce-rich compositions appear to have higher mobility than that of the Zr-rich compositions. In combination with more favorable hydration enthalpies in the barium cerates, it is almost certain that the proton conductivity of the barium cerates is superior to that of the barium zirconates. Fig. 11a – 11c demonstrates the published data of proton conductivities of the doped $BaZrO_3$, $BaCeO_3$, and $BaCe_{1-x}Zr_xO_3$, respectively.

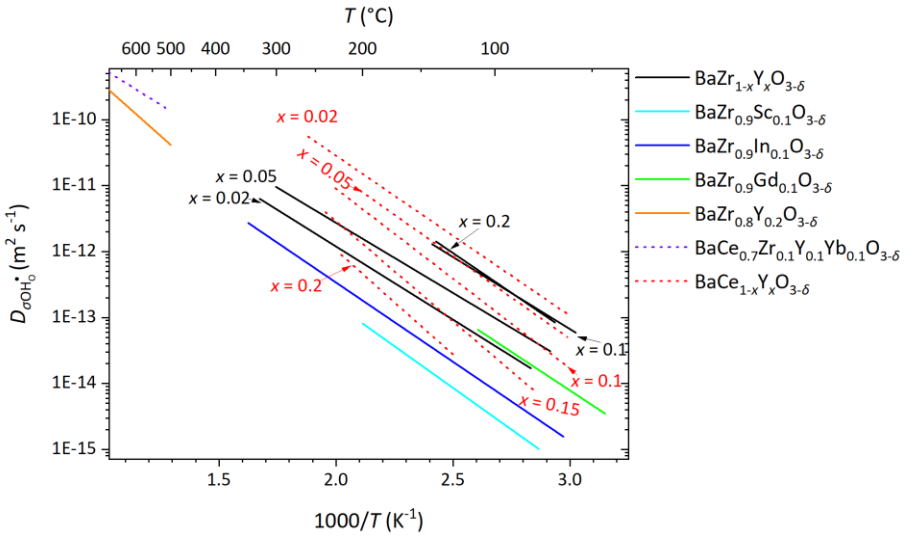

Fig. 10 Proton diffusion coefficient ($D_{\sigma_{OH_O^\bullet}}$) of doped $BaCeO_3$(dotted lines)- and $BaZrO_3$(solid lines)-based proton conductors. Data of $D_{\sigma_{OH_O^\bullet}}$ of $BaZr_{1-x}Y_xO_{3-\delta}$, $BaZr_{0.9}Sc_{0.1}O_{3-\delta}$, $BaZr_{0.9}In_{0.1}O_{3-\delta}$, and $BaZr_{0.9}Gd_{0.1}O_{3-\delta}$ were taken from ref. [117], $BaCe_{1-x}Y_xO_{3-\delta}$ from ref. [119], $BaZr_{0.8}Y_{0.2}O_{3-\delta}$ from ref. [122] and $BaCe_{0.7}Zr_{0.1}Y_{0.1}Yb_{0.1}O_{3-\delta}$ from ref [126].

For both $BaZrO_3$-based and $BaCeO_3$-based electrolyte materials, the proton conductivity of Y doped compositions displays the highest values due to favorable hydration and migration energies. Gilardi *et al*. also pointed out that coordination to the Y and the Zr cations was one of the main reasons for the unique proton transport properties of Y-doped $BaZrO_3$.[133]

Indeed, the proton conductivities of the Ce-rich compositions are generally higher than those of the zirconates. However, the poor chemical stability of the cerates limited their application as

electrolytes. Efforts have been made to improve the chemical stability of the cerates through doping The following section will focus on the effect of dopants on the stability of the barium cerates.

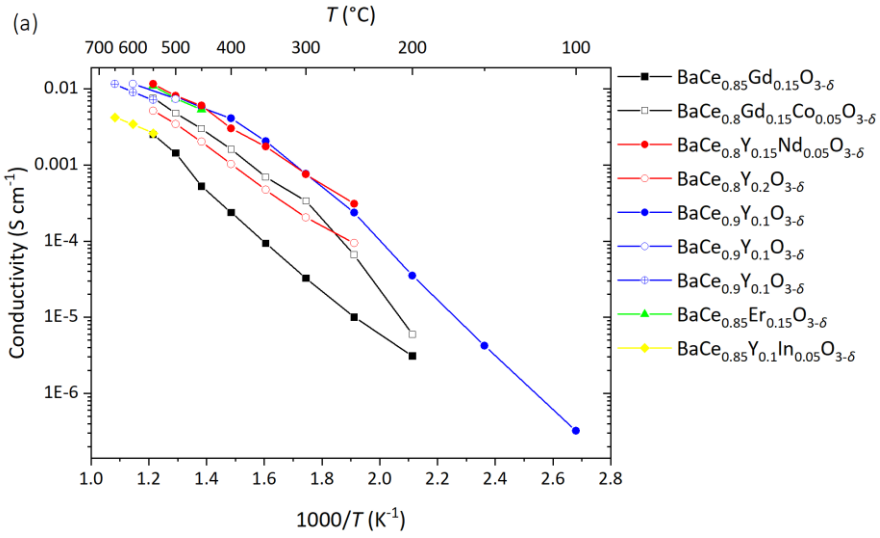

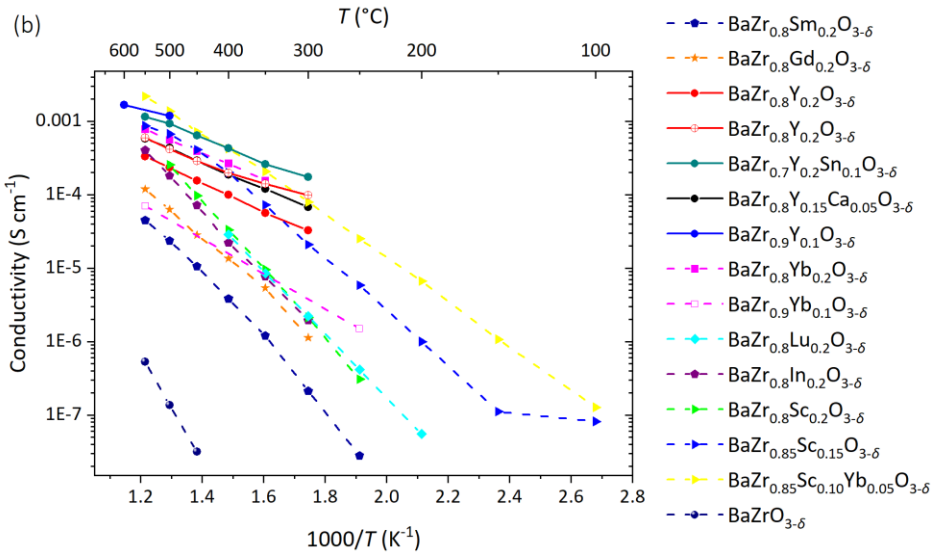

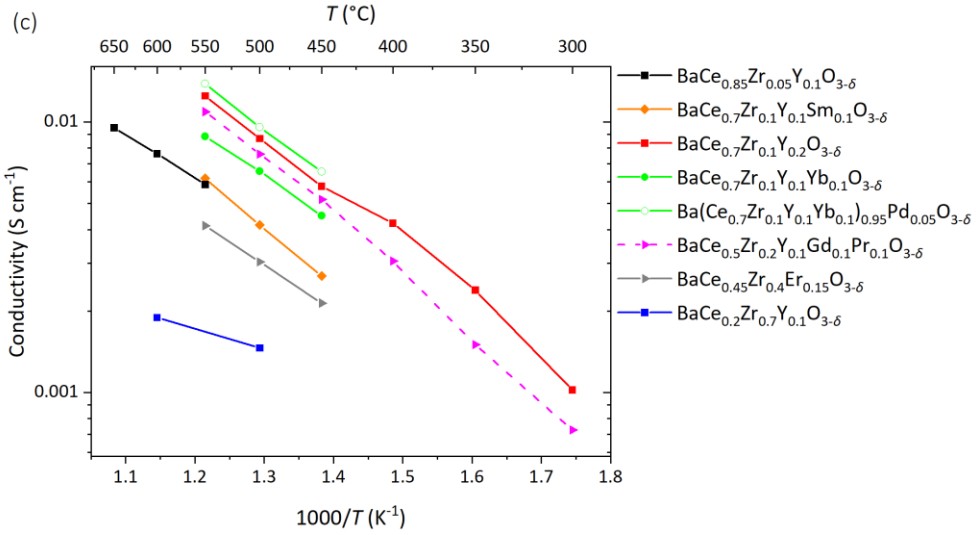

Fig. 11 Proton conductivity of (a) $BaZrO_3$-, (2) $BaCeO_3$- and (3) $BaCe_{1-x}Zr_xO_3$- based proton conductors. Solid lines are conductivity data obtained in humidified (usually p_{H_2O} = 0.033 atm) H_2, while dotted lines represent those obtained in humidified Ar or N_2. Data of proton conductivity of $BaCe_{0.9}Gd_{0.1}O_{3-\delta}$ and $BaCe_{0.85}Co_{0.05}Gd_{0.1}O_{3-\delta}$ are from ref. [134], $BaCe_{0.8}Y_{0.2}O_{3-\delta}$ and $BaCe_{0.8}Y_{0.15}Nd_{0.05}O_{3-\delta}$ from ref. [102], $BaCe_{0.8}Y_{0.2}O_{3-\delta}$ from ref. [121, 135, 136], $BaCe_{0.85}Er_{0.15}O_{3-\delta}$ from ref. [111], $BaCe_{0.85}Y_{0.1}In_{0.05}O_{3-\delta}$ from ref. [135], $BaZrO_{3-\delta}$, $BaZr_{0.8}In_{0.2}O_{3-\delta}$, $BaZr_{0.8}Sc_{.2}O_{3-\delta}$, $BaZr_{0.8}Lu_{0.2}O_{3-\delta}$, $BaZr_{0.8}Gd_{0.2}O_{3-\delta}$ and $BaZr_{0.8}Sm_{0.2}O_{3-\delta}$ from ref. [133], $BaZr_{0.8}Y_{0.2}O_{3-\delta}$ from ref. [107, 133], $BaZr_{0.9}Y_{0.1}O_{3-\delta}$ from ref. [121], $BaZr_{0.7}Sn_{0.1}Y_{0.2}O_{3-\delta}$ from ref. [138], $BaZr_{0.80}Y_{0.15}Ca_{0.05}O_{3-\delta}$ from ref. [107], $BaZr_{0.8}Yb_{0.2}O_{3-\delta}$ and $BaZr_{0.9}Yb_{0.1}O_{3-\delta}$ from ref. [139], $BaZr_{0.85}Sc_{0.15}O_{3-\delta}$ and $BaZr_{0.85}Sc_{0.10}Yb_{0.05}O_{3-\delta}$ from ref. [140], $BaCe_{0.85}Zr_{0.05}Y_{0.1}O_{3-\delta}$ from ref. [135], $BaCe_{0.7}Zr_{0.1}Y_{0.2}O_{3-\delta}$ from ref. [110], $BaCe_{0.2}Zr_{0.7}Y_{0.1}O_{3-\delta}$ from ref. [121], $BaCe_{0.7}Zr_{0.1}Y_{0.1}Sm_{0.1}O_{3-\delta}$ from ref. [141], $BaCe_{0.5}Zr_{0.2}Y_{0.1}Gd_{0.1}Pr_{0.1}O_{3-\delta}$ from ref. [142], $BaCe_{0.7}Zr_{0.1}Y_{0.1}Yb_{0.1}O_{3-\delta}$ and $Ba(Ce_{0.7}Zr_{0.1}Y_{0.1}Yb_{0.1})_{0.95}Pd_{0.05}O_{3-\delta}$ from ref. [143],and $BaCe_{0.45}Zr_{0.4}Er_{0.15}O_{3-\delta}$ from ref. [111].

3.2.2. Chemical stability

As stated above the acceptor-doped $BaZrO_3$ exhibits high chemical stability against H_2O and CO_2.[144-148] Efforts have been made on mixing acceptor-doped $BaZrO_3$ with $BaCeO_3$ to improve the overall chemical stability of the mixture while preserving the high proton conductivity. Fig. 11 demonstrated that the proton conductivity of the acceptor-doped $BaCe_{1-x}Zr_xO_3$ is indeed higher than the acceptor-doped $BaZrO_3$ and is generally proportional to the Ce concentration. Shown in Fig. 12a, Tu *et al*. studied the chemical stability of $BaZr_{0.8-x}Ce_xY_{0.2}O_3$ (x = 0, 0.2, 0.3 and 0.4) under pure CO_2 environment, and found that only $BaZr_{0.8-x}Ce_xY_{0.2}O_3$ ($x \leq 0.2$) compositions are chemically stable up to 1000 °C while $x > 0.2$ compositions decompose and form $BaCO_3$ above 550 °C.[144] Similarly, Sawant *et al*. found that the decomposition of $BaZr_{0.8-x}Ce_xY_{0.2}O_3$ happens when the Ce concentration is higher than 40%, as shown in Fig. 12b. Zhong demonstrated that only with Ce concentrations below 50 %, $BaZr_{0.9-x}Ce_xY_{0.1}O_3$ are stable in a pure CO_2 at 900 °C.[149] For most $BaZr_{1-x}Ce_xO_3$ systems, x needs to be below 0.4-0.6 for them to be stable in CO_2 rich environments, the exact limit depending on the co-dopants used and the temperature.[150-152] Others attempted to use various acceptor ions, such as La^{3+}, Pr^{3+}, Nd^{3+}, Sm^{3+}, Gd^{3+}, Y^{3+}, Tm^{3+}, Yb^{3+}, Lu^{3+}, In^{3+}, Sc^{3+}, to improve the chemical stability of the $BaCeO_3$ in the H_2O and CO_2-rich environments.[135, 142, 153-158] It is shown that the chemical stability of the acceptor-doped $BaCeO_3$ in a moist- and CO_2-rich environments improves with the increasing electronegativity of the acceptor dopants. The electronegativities of the aforementioned acceptor dopants are listed in Table 4. For instance, with a significantly higher electronegativity of In

(1.78) than Ce (1.12), the chemical stability of In-doped $BaCeO_3$ against CO_2 and moisture has been drastically improved.[135, 156] However, it was also discovered that the high-electronegativity dopant can lead to unfavourable hydration energy, as mentioned above. Therefore, there is a trade-off between improving proton conductivity and chemical stability when choosing the dopant element.

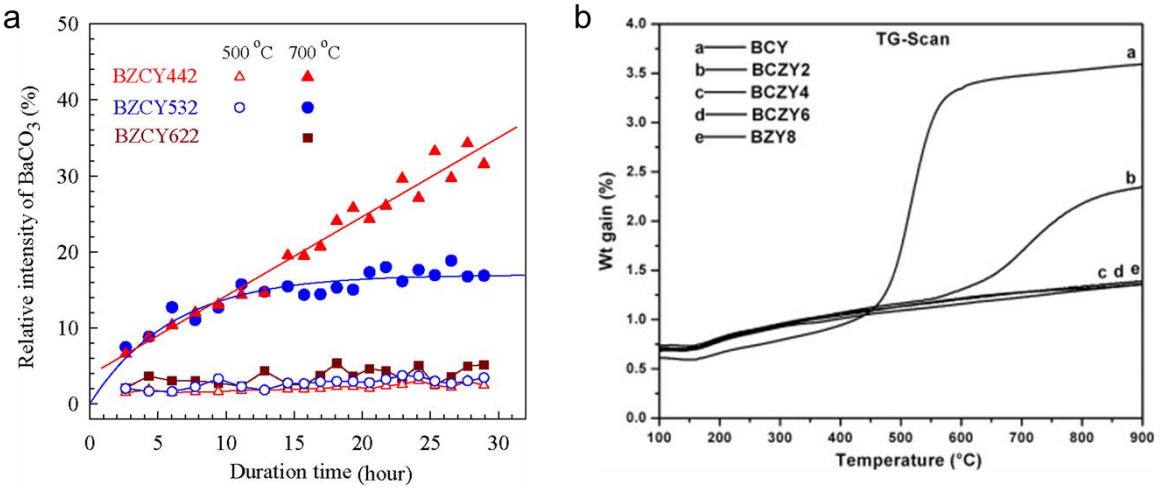

Fig. 12 Resistance of the $BaCe_{0.8-x}Zr_xY_{0.2}O_{3-\delta}$ (BCZY) composition to CO_2 measured by monitoring (a) relative intensity of $BaCO_3$ peak at ϑ = 24° and (110) peak of BCZY at 500 and 700 °C Reprinted with permission from [144], (b) mass change of the BCZY (number denotes the Zr content, e.g. BCZY2 is $BaCe_{0.6}Zr_{0.2}Y_{0.2}O_{3-\delta}$) under CO_2 atmosphere from 100 to 900 °C. Reprinted with permission from [159]

Table 4 Electronegativity of the acceptor-type dopant elements for $BaCeO_3$

Elements	La	Yb	Ce*	Pr	Nd	Sm	Gd	Y	Er	Lu	Zr*	Sc	In	Ga
Electronegativity	1.1	1.1	1.12	1.13	1.14	1.17	1.2	1.22	1.24	1.27	1.33	1.36	1.78	1.81

* Elements that have the valence of +4.

Similarly, high-valence, high-electronegativity dopants, such as Sn^{4+}, Nb^{5+}, Ta^{5+}, can also effectively stabilize the $BaCeO_3$ structures.[160-164] Improving the proton conductivity and chemical stability with increasing the donor-dopant concentrations is a trade-off against lower oxygen vacancy concentration and less favourable hydration energy. While some of the low-level isovalent- or donor-doped $BaCeO_3$ materials shows proton conductivity, e.g. σ = 4.1 mS cm^{-1} at 550 °C for $BaCe_{0.87}Ta_{0.03}Y_{0.1}O_{3-\delta}$, the proton conductivities are lower than those of the acceptor-doped ones.[160]

3.2.3. Sinterability and microstructure

The sinterability of perovskite-type proton conductors has been intensively studied in the past years. Improved sinterability not only improves the densification of the electrolyte layer but also increases the grain size, therefore decreasing the amount of grain boundaries. It has been observed by many researchers that both the resistance and energy barrier of proton conduction on grain

boundary are significantly higher than those in the bulk in the $BaZrO_3$-based electrolyte materials.[143, 145, 150, 159] The sluggish proton conductivity across grain boundary is believed to arise from the space charge depletion zone which is adjacent to the grain boundary. [106, 109, 135, 165-167] The space charge depletion zone, as illustrated in Fig. 13, is believed to be caused by a positive excess charge builds up in the grain boundary core, leading to a depletion of all mobile positive charge carriers including $OH_O^{\bullet}$ and $V_O^{\bullet\bullet}$.[166, 168, 169] Therefore, a material with a favoured sinterability is beneficial not only for its processability but also for its proton conductivity.

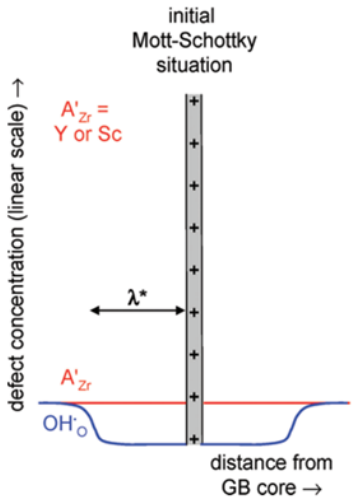

Fig. 13 Schematic drawing of dopant (A'_{Zr}) and proton concentrations ($OH_O^{\bullet}$) at a grain boundary of an as-prepared sample. (Mott-Schottky situation: constant dopant concentration, core charge exclusively compensated by proton depletion). Reprinted with permission from [169]

Notably, the powder synthesis method is of vital importance to the sinterability of the material, as it affects the particle size, geometry, and homogeneity of the powder. In addition, the sintering temperature, time and method can significantly affect the sintering properties of the samples and consequently the resulting microstructure. Such factors will not be discussed, as many excellent reviews are available.[170-172] In Table 5, we summarize the literature data of sintering properties and grain sizes of the acceptor-doped $BaZrO_3$, $BaCeO_3$, and $BaCe_{1-x}Zr_xO_3$ electrolyte materials, and elucidate the influence of dopant ions on the sinterability and microstructure. The acceptor-doped $BaZrO_3$ generally requires a high sintering temperature at 1650 – 1700 °C to obtain a sample with a relative density higher than 94%, while the acceptor-doped $BaCeO_3$ only needs a sintering temperature of 1400 – 1550 °C. Sawant *et al*. attempted to sinter the $BaCe_{0.8-x}Zr_xY_{0.2}O_3$ (x = 0.0, 0.2, 0.4, 0.6 and 0.8) at 1400 °C for 10 hours in the air, and they found that both, the relative density and grain size decreased with increasing Zr content (shown in Fig. 14), requiring a trade-off between

chemical stability and sinterability.[159] Small acceptor-type ions, such as Ga, Sc, and In, improve the sinterability of the $BaZrO_3$ and result in relatively large and uniform grains.[140, 173] However, barium zirconate doped with such elements also results in a lower proton conductivity due to the high electronegativity of the corresponding ions. Doping with larger cations, such as Y, Yb, and Gd, results in a relatively lower relative density sample with small and non-uniform grains, despite that the Y or Yb doped $BaCeO_3$ and $BaCe_{1-x}Zr_xO_3$ showed the highest proton conductivities.[110, 121, 136, 143] It is noteworthy that densification of the large-acceptor doped barium zirconates can eventually be achieved by prolonged sintering (24 – 100 h) at elevated temperature.[174, 175] However, this is believed to reduce the total proton conductivity in barium zirconates due to (1) larger space charge depletion zone created by more segregation in the grain boundary, (2) alteration of the initial stoichiometry due to evaporation of Ba during sintering. Therefore, the most-used strategy nowadays to improve the sintering results of barium zirconates, besides optimizing the synthesis method of the powders and the sintering technique, is by using oxide additions, such as NiO, CuO, ZnO. The sintering aids provide an eutectic phase, that reduces the required sintering temperature of the $BaCeO_3$ and $BaCe_{1-x}Zr_xO_3$ electrolyte materials down to 1300 – 1400 °C. Nevertheless, many researchers have found that the application of sintering aids is detrimental to the electrochemical properties.[176-183] To further understand the influence of sintering aids on electrolyte performance, the reader is referred to other excellent reviews in the field.[172, 184, 185]

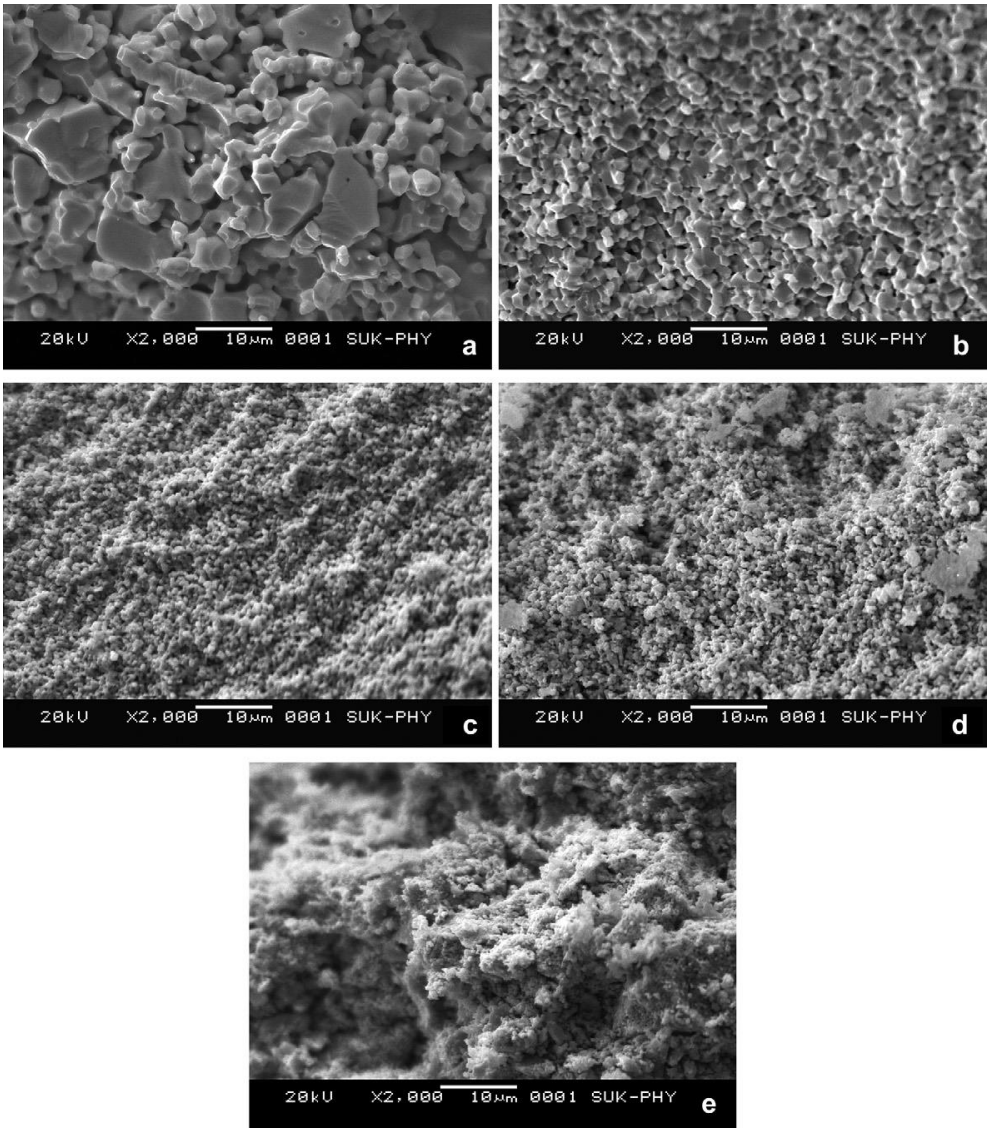

Fig. 14 SEM images of fracture surface of: (a) $BaCe_{0.8}Y_{0.2}O_3$; (b) $BaCe_{0.6}Zr_{0.2}Y_{0.2}O_3$; (c) $BaCe_{0.4}Zr_{0.4}Y_{0.2}O_3$; (d) $BaCe_{0.2}Zr_{0.6}Y_{0.2}O_3$, (e) $BaZr_{0.8}Y_{0.2}O_3$ sintered at 1400 °C for 10 h in air. Reprinted with permission from [159]

Table 5 Relative density and average grain size of various acceptor-doped $BaZrO_3$, $BaCeO_3$, and $BaCe_{1-x}Zr_xO_3$ electrolyte materials obtained using different sintering temperatures and sintering times.

Electrolyte materials	Synthesis method	Sintering temperature/°C	Sintering time /h	Relative density	Grain size /μm	Ref.
$BaZrO_{3-\delta}$	SSR	1600	24	96.0%	2	[186]
$BaZr_{0.98}Y_{0.02}O_{3-\delta}$				95.0%	1-2	
$BaZr_{0.95}Y_{0.05}O_{3-\delta}$				98.0%	<0.5	
$BaZr_{0.9}Y_{0.1}O_{3-\delta}$				93.0%	0.2-1	
$BaZr_{0.85}Y_{0.15}O_{3-\delta}$				92.0%	<0.2	
$BaZr_{0.8}Y_{0.2}O_{3-\delta}$				96.0%	1.5-2	

$BaZr_{0.75}Y_{0.25}O_{3-\delta}$				96.0%	2-4	
$BaZr_{0.7}Y_{0.3}O_{3-\delta}$				96.0%	1-2	
$BaZr_{0.9}Sc_{0.1}O_{3-\delta}$	SSR	1650	-	91.0%		[117]
$BaZr_{0.9}In_{0.1}O_{3-\delta}$		1700	-	93.0%		
$BaZr_{0.9}Y_{0.1}O_{3-\delta}$				91.0%		
$BaZr_{0.9}Gd_{0.1}O_{3-\delta}$				88.0%		
$BaZr_{0.98}Y_{0.02}O_{3-\delta}$				95.0%		
$BaZr_{0.95}Y_{0.05}O_{3-\delta}$				97.0%		
$BaZr_{0.85}Y_{0.15}O_{3-\delta}$				90.0%		
$BaZr_{0.8}Y_{0.2}O_{3-\delta}$				92.0%		
$BaZr_{0.75}Y_{0.25}O_{3-\delta}$				87.0%		
$BaZr_{0.9}Y_{0.1}O_{3-\delta}$	SSR	1700	6	90.0%		[121]
$BaZr_{0.9}Y_{0.1}O_{3-\delta}$	SSR	1700	10	82.5%		[173]
$BaZr_{0.9}Y_{0.05}In_{0.05}O_{3-\delta}$				97.5%		
$BaZr_{0.9}In_{0.1}O_{3-\delta}$				97.0%		
$BaZr_{0.9}Y_{0.05}Ga_{0.05}O_{3-\delta}$				94.0%		
$BaZr_{0.9}Ga_{0.1}O_{3-\delta}$				95.5%		
$BaZr_{0.9}Yb_{0.1}O_{3-\delta}$	SSR	1500	48	70.0%		[187]
$BaZr_{0.95}Yb_{0.05}O_{3-\delta}$	SSR	1600	12	95.3%		[139]
$BaZr_{0.9}Yb_{0.1}O_{3-\delta}$				91.4%		
$BaZr_{0.8}Yb_{0.2}O_{3-\delta}$				83.2%		
$BaZr_{0.85}Sc_{0.15}O_{3-\delta}$	SSR	1600	24	92.0%		[140]
$BaZr_{0.85}Sc_{0.10}Yb_{0.05}O_{3-\delta}$				91.0%		
$BaZr_{0.85}Sc_{0.05}Yb_{0.10}O_{3-\delta}$				90.0%		
$BaZr_{0.8}Y_{0.2}O_{3-\delta}$	Citric-nitrate combustion	1600	8	90.0%		[133]
$BaZr_{0.8}In_{0.2}O_{3-\delta}$				94.0%		
$BaZr_{0.8}Sc_{0.2}O_{3-\delta}$				76.0%		
$BaZr_{0.8}Lu_{0.2}O_{3-\delta}$				76.0%		
$BaZr_{0.8}Gd_{0.2}O_{3-\delta}$				94.0%		
$BaZr_{0.8}Sm_{0.2}O_{3-\delta}$				94.0%		
$BaZr_{0.8}Y_{0.2}O_{3-\delta}$	Modified combustion	1650	10	80.0%		[138]
$BaZr_{0.7}Sn_{0.1}Y_{0.2}O_{3-\delta}$				83.0%		
$BaZr_{0.8}Y_{0.2}O_{3-\delta}$	SSRS + ball milling	1435	5	56.0%	0.51	[174]
			15	70.0%	0.72	
		1485	10	82.0%	0.88	
		1535	5	87.0%	1.02	
			15	94.0%	1.19	
$BaCeO_{3-\delta}$	SSR	1400	6	>90%	4.4	[155]
$BaCe_{0.9}Gd_{0.1}O_{3-\delta}$		1400	6	>90%	1.4	
$BaCe_{0.9}Nd_{0.1}O_{3-\delta}$		1400	6	>90%	1.8	

$BaCe_{0.9}Sm_{0.1}O_{3-\delta}$		1400	6	>90%	2.2	
$BaCe_{0.9}Y_{0.1}O_{3-\delta}$		1400	6	>90%	1.6	
$BaCe_{0.85}Gd_{0.15}O_{3-\delta}$	Citrate-nitrate combustion	1500	5	-	3-10	[134]
$BaCe_{0.82}Co_{0.03}Gd_{0.15}O_{3-\delta}$				-	20	
$BaCe_{0.8}Co_{0.05}Gd_{0.15}O_{3-\delta}$				99.5%	≤50	
$BaCe_{0.85}Er_{0.15}O_{3-\delta}$	Microemulsion route	1550	10	93.0%		[111, 188]
$BaCe_{0.95}Sm_{0.05}O_{3-\delta}$	SSR	1600	3	87.0%	1	[189]
$BaCe_{0.9}Sm_{0.1}O_{3-\delta}$				94.0%	3	
$BaCe_{0.85}Sm_{0.15}O_{3-\delta}$				94.0%	4	
$BaCe_{0.95}Y_{0.05}O_{3-\delta}$	SSR	1550	3	89.0%	2	
$BaCe_{0.9}Y_{0.1}O_{3-\delta}$				98.0%	10	
$BaCe_{0.85}Y_{0.1}In_{0.05}O_{3-\delta}$	Citrate-nitrate combustion	1400	-	94.0%	1	[135]
$BaCe_{0.9}Y_{0.1}O_{3-\delta}$		1550	-	96.0%	1.5	
$BaCe_{0.85}Y_{0.1}Zr_{0.05}O_{3-\delta}$		1550	-	93.0%	1.2	
$BaCe_{0.85}Y_{0.1}Nb_{0.05}O_{3-\delta}$		1550	-	92.0%	1.3	
$BaCe_{0.9}Y_{0.1}O_{3-\delta}$	SSR	1700	6	95.0%		[121]
$BaCe_{0.7}Zr_{0.1}Y_{0.1}Yb_{0.1}O_{3-\delta}$	(EDTA)-citric acid complexing	1500	10	94.0%		[143]
$Ba(Ce_{0.7}Zr_{0.1}Y_{0.1}Yb_{0.1})_{0.95}Pd_{0.05}O_{3-\delta}$		1400	10	98.0%		
$BaCe_{0.45}Zr_{0.4}Er_{0.15}O_{3-\delta}$	Microemulsion route	1550	10	93.0%		[111]
$BaCe_{0.8}Y_{0.2}O_{3-\delta}$	Sol-gel method	1400	10	96.3%	3-8	[159]
$BaCe_{0.6}Zr_{0.2}Y_{0.2}O_{3-\delta}$				95.5%	2-3	
$BaCe_{0.4}Zr_{0.4}Y_{0.2}O_{3-\delta}$				93.5%	0.5-1	
$BaCe_{0.2}Zr_{0.6}Y_{0.2}O_{3-\delta}$				89.6%	0.2-0.5	
$BaZr_{0.8}Y_{0.2}O_{3-\delta}$				78.3%	<0.1	
$BaCe_{0.2}Zr_{0.7}Y_{0.1}O_{3-\delta}$	SSR	1700	6	92.0%	-	[121]
$BaCe_{0.6}Zr_{0.3}Y_{0.1}O_{3-\delta}$				93.0%	-	
$BaCe_{0.5}Zr_{0.3}Y_{0.05}Yb_{0.1}Zn_{0.05}O_{3-\delta}$	SSR	1500	10	99.7%	1-3	[190]
$BaCe_{0.5}Zr_{0.3}Yb_{0.15}Zn_{0.05}O_{3-\delta}$				98.8%	5	

3.2.4. Performance of proton conducting electrolyte in LT-SOCs

Recent results of the performance of the SOCs that use proton conducting electrolyte at below 600 °C are summarized in Table 6. SOCs operate either in protonic conducting fuel cell (PCFC) mode, or protonic conducting electrolyzer cell (PCEC) mode, or reversible mode (PCFC/PCEC). The peak power density (P_{max}) is obtained in the PCFC mode, while current density at thermal neutral voltage (i_{TNV}) is used to evaluate the performance of the cells in the PCEC mode. The performance of the electrolyte layer is evalued by the ohmic resistance that is normally measured by electrochemical impedance spectroscopy (EIS). The The electrolyte materials, except for a few new derivatives of barium cerates/zirconates like $BaHf_{0.3}Ce_{0.5}Y_{0.1}Yb_{0.1}O_{3-\delta}$ [191] and $SrZr_{0.5}Ce_{0.4}Y_{0.1}O_{2.95}$ [192], are by and large $BaCe_{1-x}Zr_xY_{0.2}O_{3-\delta}$ and $BaCe_{1-x}Zr_x Y_{0.1}Yb_{0.1}O_{3-\delta}$ compositions due to their balanced chemical stability, sinterability and proton conductivity. To further minimize the ohmic drop across the electrolyte, the electrolyte layer in most of the recently published works have been reduced to around 10 µm.[193-199] With such thin electrolyte layers, the ohmic resistance can be controlled to as low as 0.2 Ω cm^2 at 500 °C. The techniques to produce thin electrolyte layers have been elucidated above. Li *et al*. reported a remarkable µ-SOFC system with the electrolyte layer down to 75 nm using the PLD technique. The ohmic resistance is limited to merely 0.099 at 350 °C. However, at such low temperature, the thermally-driven oxygen evolution reaction (OER) kinetics becomes the rate-determing proess among the entire cell reactions. Therefore, the challenge of developing LT-SOCs lies not only on developing high-performance and cost-effective electrolyte layer but also on selecting catalytically more active oxygen electrode materials to promote the OER kinetics.

Table 6 Performance of the solid oxide fuel/electrolyzer cells (peak power density, P_{max}, current density at thermal neutral voltage, i_{TNV}, and open circuit voltage, OCV) at below 600 °C using different electrolyte materials with their ohmic and polarization resistance.

Electrolyte materials	Cathode materials	Electrolyte thickness (µm)	Operating mode	Operating temperature (°C)	Ohmic resistance, R_o (Ω cm^2)	Polarization resistance, R_p (Ω cm^2)	OCV (V)	P_{max} (mW cm^{-2})	i_{TNV} (A cm^{-2})*	Ref
$BaZr_{0.8}Y_{0.2}O_{3-\delta}$	$Sm_{0.5}Sr_{0.5}CoO_{3-\delta}$ nanoparticles	15	PCFC	500	-	-	-	250	-	[194]
				550	-	-	-	390	-	
				600	0.22	0.085	-	601	-	
$BaZr_{0.8}Y_{0.2}O_{3-\delta}$	Pt	0.075	PCFC	350	0.099	11.899	-	51	-	[200]
				375	0.089	7.045	-	93	-	
				400	0.085	3.66	1.02	206	-	

$BaCe_{0.4}Zr_{0.4}Y_{0.2}O_{3-\delta}$ + 1 wt% ZnO	$La_{0.8}Sr_{0.2}Co_{0.7}Ni_{0.3}O_{3-\delta}$	24	PCFC/ PCEC	500	0.307	0.43	1.09	409	0.327	[198]
				550	-	0.19	-	652	0.684	
				600	0.202	0.09	1.05	882	1.09	
$BaCe_{0.4}Zr_{0.4}Y_{0.1}Yb_{0.1}O_{3-\delta}$	$PrNi_{0.5}Co_{0.5}O_{3-\delta}$	15	PCFC/ PCEC	400	0.787	0.60	-	-	0.07	[197]
				450	0.575	0.35	-	-	0.125	
				500	0.408	0.13	-	§230	0.36	
				550	0.292	0.08	-	§354	0.488	
				600	0.19	0.03	1.06	§528	0.86	
$BaCe_{0.4}Zr0.4Y_{0.1}Yb_{0.1}O_{3-\delta}$	$PrBa_{0.5}Sr_{0.5}Co_{1.5}Fe_{0.5}O_{5+\delta}$	20	PCFC/ PCEC	500	0.3	0.66	1.08	370	0.382	[195]
				550	0.22	0.25	1.07	594	0.78	
				600	0.18	0.14	1.05	825	1.399	
$BaCe_{0.5}Zr_{0.3}Y_{0.1}Yb_{0.1}O_{3-\delta}$	$BaCe_{0.1}Zr_{0.2}Y_{0.1}Fe_{0.6}O_{3-\delta}$	30	PCFC	600	0.89	1.52	1.102	74	-	[201]
$BaCe_{0.7}Zr_{0.1}Y_{0.1}Yb_{0.1}O_{3-\delta}$	$Ba_{0.95}La_{0.05}Fe_{0.8}Zn_{0.2}O_{3-\delta}$ - 30 wt% BCZYYb	42	PCFC	600	0.63	0.07	1.03	142.8	-	[196, 202]
$BaCe_{0.7}Zr_{0.1}Y_{0.2}O_{3-\delta}$	$Ba_{0.9}Co_{0.4}Fe_{0.4}Zr_{0.1}Y_{0.1}O_{3-\delta}$ - $BaZr_{0.1}Ce_{0.7}Y_{0.2}O_{3-\delta}$	25	PCFC	550	0.48	1.45	-	150	-	[196]
				600	0.37	0.65	-	240	-	
$BaCe_{0.7}Zr_{0.1}Y_{0.2}O_{3-\delta}$	$Ba_{0.95}Ca_{0.05}Fe_{0.85}Sn_{0.05}Y_{0.1}O_{3-\delta}$ - 30 wt% SDC	-	PCFC	550	0.27	0.57	1.035	303	-	[203]
				600	0.254	0.24	1.011	505	-	
$BaCe_{0.7}Zr_{0.1}Y_{0.1}Yb_{0.1}O_{3-\delta}$	$Gd_{0.3}Ca_{2.7}Co_{3.82}Cu_{0.18}O_{9-\delta}$ - 40 wt% BCZYYb	-	PCFC/ PCEC	450	0.307	0.762	-	280	-	[204]
				500	-	0.254	1.063	480	0.74	
				550	-	0.126	-	770	1.26	
				600	-	0.067	1.056	1160	2.05	
$BaCe_{0.7}Zr_{0.1}Y_{0.1}Yb_{0.1}O_{3-\delta}$	$BaCo_{0.4}Fe_{0.4}Zr_{0.1}Y_{0.1}O_{3-\delta}$	10	PCFC/ PCEC	500	0.243	0.242	-	451	0.453	[193]
				550	0.226	0.17	-	529	0.688	
				600	0.22	0.126	-	633	0.921	
$BaCe_{0.7}Zr_{0.1}Y_{0.2}O_{3-\delta}$ + 1 wt% NiO	$BaCe_{0.2}Fe_{0.6}Pr_{0.2}O_{3-\delta}$	40	PCFC	550	0.81	0.7	1.07	180	-	[205]
				600	0.59	0.22	1.04	322	-	
$BaCe_{0.7}Zr_{0.1}Y_{0.1}Yb_{0.1}O_{3-\delta}$ + 1 wt% NiO	$BaCe_{0.4}Fe_{0.4}Co_{0.2}O_{3-\delta}$	70	PCFC	600	0.92	0.26	1.097	237	-	[206]
$BaCe_{0.7}Zr_{0.1}Y_{0.1}Yb_{0.1}O_{3-}$	$Pr_{1.7}Ba_{0.3}NiO_{4+\delta}$ - 50 wt% BCZYYb	-	PCEC	550	0.367	0.21	0.984	-	0.49	[207]

$_{\delta}$ + 1 wt% ZnO										
				600	0.277	0.09	0.972	-	0.83	
$BaCe_{0.7}Zr_{0.1}Y_{0.1}Yb_{0.1}O_{3-\delta}$ + 1 wt% NiO	$PrBa_{0.8}Ca_{0.2}Co_2O_{5+\delta}$	10	PCFC/ PCEC	500	0.171	1.447	-	-	-	[199]
				550	0.129	0.447	1.1	660	0.69	
				600	0.108	0.178	1.074	1060	1.51	
$BaCe_{0.8}Y_{0.15}Nd_{0.05}O_{3-\delta}$	$SmBaCo_2O_{5+\delta}$ + $Ce_{0.8}Sm_{0.2}O_{2-\delta}$ (7:3)	20	PCFC	600	0.44	0.3	1.04	360	-	[102]
$SrZr_{0.5}Ce_{0.4}Y_{0.1}O_{2.95}$	$BaGd_{0.8}La_{0.2}Co_2O_{6-\delta}$	20	PCEC	600	1.3	-	0.77	-	0.131	[192]
$SrZr_{0.5}Ce_{0.4}Y_{0.1}O_{2.95}$	$Ba_{0.5}La_{0.5}CoO_{3-\delta}$	20	PCEC	600	1.4	-	0.79	-	0.199	[192]
$BaHf_{0.3}Ce_{0.5}Y_{0.1}Yb_{0.1}O_{3-\delta}$	$PrBa_{0.5}Sr_{0.5}Co_{1.5}Fe_{0.5}O_{5+\delta}$	10	PCFC/ PCEC	600	-	-	1.04	1070	1.55	[191]

* Thermal neutral voltage E_{TNV} = 1.3 V.

§ Power density at E = 1.3 V.

4. Conclusions

The development of LT-SOCs, defined as the operation temperature lower than 500 °C, has been discussed with a focus the potential improvements that have been reported in terms of cell structure and materials design.

The electrolyte thickness can be reduced to a nanometer scale for a low ohmic resistance of the cell, thus efficiently reducing the working temperature of SOCs. The construction of thin-film electrolytes is believed to be the most important part of the structure optimization of the LT-SOCs. PLD is the most popular method to produce a thin-film electrolyte. The formation of pinholes in the electrolyte can be avoided by applying a dense and smooth subtract or a proper functional layer design. PLD is currently limited to application on the lab-scale. Sputtering and spraying can be promising methods for upscaling thin-film electrolyte fabrication but a high-quality electrolyte needs relatively more strict process control with these technologies.. ALD is believed to be the most promising technology for the development of free-stand thin-film electrolytes and also shows unique features in supported electrolyte fabrication. Novel precursor development is the most important for the future application of the ALD process for new proton-conducting electrolyte fabrication.

The conductivity, mechanical stability, and durability of the thin-film have been improved significantly in the past decades. However, cost and productivity are the most critical factors to limit the application of thin-film electrolytes. Free-stand thin-film electrolyte is promising for the

manufacture of SOFCs operating in portable devices. The large-scale SOCs, especially electrolyzer, favorites supported thin-film electrolyte, which requires compatibility of the substrate process with the scalable thin-film coating process. Exploration of functional layer fabrication process is the most essential for the development of supported thin-film electrolyte. Other than cell structure optimization, novel electrolyte materials also promote the performance of SOCs. Especially, proton conducting ceramics with low activation energy have efficiently lowered the working temperature of SOCs to the LT range. The proton conductivity of the materials can be improved by promoting the hydration process and elevating proton mobility in the oxide. Doping is an effective method to optimize the performance of these protons conducting ceramics. Perovskite-type $BaCeO_3$- and $BaZrO_3$-based oxides are the most widely studied electrolyte materials for LT-SOCs. The stability of Ce-rich oxides under H_2O or CO_2 containing atmosphere and the sinterability of $BaZrO_3$ in the membrane fabrication need to be optimized.

References

[1] R. Rosli, A. Sulong, W. Daud, M. Zulkifley, T. Husaini, M. Rosli, E. Majlan, and M. Haque, A review of high-temperature proton exchange membrane fuel cell (HT-PEMFC) system, *Int. J. Hydrogen Energy*, 42 (2017), No. 14, p. 9293.

[2] Z. Liu, M. Zhou, M. Chen, D. Cao, J. Shao, M. Liu, and J. Liu, A high-performance intermediate-to-low temperature protonic ceramic fuel cell with in-situ exsolved nickel nanoparticles in the anode, *Ceram. Int.*, 46 (2020), No. 12, p. 19952.

[3] H. Ding, W. Wu, C. Jiang, Y. Ding, W. Bian, B. Hu, P. Singh, C.J. Orme, L. Wang, Y. Zhang, and D. Ding, Self-sustainable protonic ceramic electrochemical cells using a triple conducting electrode for hydrogen and power production, *Nat. Commun.*, 11 (2020), No. 1, p. 1907.

[4] R. Raza, B. Zhu, A. Rafique, M.R. Naqvi, and P. Lund, Functional ceria-based nanocomposites for advanced low-temperature (300–600 °C) solid oxide fuel cell: A comprehensive review, *Mater. Today Energy*, 15 (2020), p. 100373.

[5] Y. Meng, J. Gao, Z. Zhao, J. Amoroso, J. Tong, and K.S. Brinkman, Review: recent progress in low-temperature proton-conducting ceramics, *J Mater Sci*, 54 (2019), No. 13, p. 9291.

[6] Y. Meng, J. Gao, H. Huang, M. Zou, J. Duffy, J. Tong, and K.S. Brinkman, A high-performance reversible protonic ceramic electrochemical cell based on a novel Sm-doped $BaCe_{0.7}Zr_{0.1}Y_{0.2}O_{3-\delta}$ electrolyte, *J. Power Sources*, 439 (2019), p. 227093.

[7] H.-S. Noh, J. Hong, H. Kim, K.J. Yoon, B.-K. Kim, H.-W. Lee, J.-H. Lee, and J.-W. Son, Scale-Up of Thin-Film Deposition-Based Solid Oxide Fuel Cell by Sputtering, a Commercially Viable Thin-Film Technology, *J. Electrochem. Soc.*, 163 (2016), No. 7, p. F613.

[8] H.-S. Noh, K.J. Yoon, B.-K. Kim, H.-J. Je, H.-W. Lee, J.-H. Lee, and J.-W. Son, Thermo-mechanical stability of multi-scale-architectured thin-film-based solid oxide fuel cells assessed by thermal cycling tests, *J. Power Sources*, 249 (2014), p. 125.

[9] I. Garbayo, D. Pla, A. Morata, L. Fonseca, N. Sabaté, and A. Tarancón, Full ceramic micro solid oxide fuel cells: towards more reliable MEMS power generators operating at high temperatures, *Energy Environ. Sci.*, 7 (2014), No. 11, p. 3617.

[10] H. Huang, M. Nakamura, P. Su, R. Fasching, Y. Saito, and F.B. Prinz, High-performance ultrathin solid oxide fuel cells for low-temperature operation, *J. Electrochem. Soc.*, 154 (2006), No. 1, p. B20.

[11] B.-K. Lai, K. Kerman, and S. Ramanathan, Nanostructured $La_{0.6}Sr_{0.4}Co_{0.8}Fe_{0.2}O_3/Y_{0.08}Zr_{0.92}O_{1.96}/La_{0.6}Sr_{0.4}Co_{0.8}Fe_{0.2}O_3$ (LSCF/YSZ/LSCF) symmetric thin film solid oxide fuel cells, *J. Power Sources*, 196 (2011), No. 4, p. 1826.
[12] K. Bae, D.Y. Jang, H.J. Choi, D. Kim, J. Hong, B.-K. Kim, J.-H. Lee, J.-W. Son, and J.H. Shim, Demonstrating the potential of yttrium-doped barium zirconate electrolyte for high-performance fuel cells, *Nat. Commun.*, 8 (2017), No. 1, p. 14553.
[13] J.W. Shin, D. Go, S.H. Kye, S. Lee, and J. An, Review on process-microstructure-performance relationship in ALD-engineered SOFCs, *J. Phys.: Energy*, 1 (2019), No. 4, p. 042002.
[14] Z. Fan, and F.B. Prinz, Enhancing oxide ion incorporation kinetics by nanoscale yttria-doped ceria interlayers, *Nano Lett.*, 11 (2011), No. 6, p. 2202.
[15] H. Yang, H. Lee, Y. Lim, and Y.B. Kim, Atomic layer deposition of GDC cathodic functional thin films for oxide ion incorporation enhancement, *J. Am. Ceram. Soc.*, 104 (2021), No. 1, p. 86.
[16] C. Bernay, A. Ringuedé, P. Colomban, D. Lincot, and M. Cassir, Yttria-doped zirconia thin films deposited by atomic layer deposition ALD: a structural, morphological and electrical characterisation, *J. Phys. Chem. Solids*, 64 (2003), No. 9, p. 1761.
[17] J.D. Baek, K.-Y. Liu, and P.-C. Su, A functional micro-solid oxide fuel cell with a 10 nm-thick freestanding electrolyte, *J. Mater. Chem. A* . 5 (2017), No. 35, p. 18414.
[18] K. Kerman, and S. Ramanathan, Performance of solid oxide fuel cells approaching the two-dimensional limit, *J. Appl. Phys.*, 115 (2014), No. 17, p. 174307.
[19] E.D. Wachsman, and K.T. Lee, Lowering the temperature of solid oxide fuel cells, *Science*, 334 (2011), No. 6058, p. 935.
[20] R. Nédélec, S. Uhlenbruck, D. Sebold, V.A.C. Haanappel, H.P. Buchkremer, and D. Stöver, Dense yttria-stabilised zirconia electrolyte layers for SOFC by reactive magnetron sputtering, *J. Power Sources*, 205 (2012), p. 157.
[21] H. Wang, W. Ji, L. Zhang, Y. Gong, B. Xie, Y. Jiang, and Y. Song, Preparation of YSZ films by magnetron sputtering for anode-supported SOFC, *Solid State Ionics*, 192 (2011), No. 1, p. 413.
[22] E. Kelder, O. Nijs, and J. Schoonman, Low-temperature synthesis of thin films of YSZ and $BaCeO_3$ using electrostatic spray pyrolysis (ESP), *Solid State Ion.*, 68 (1994), No. 1-2, p. 5.
[23] B. Ksapabutr, T. Chalermkiti, S. Wongkasemjit, and M. Panapoy, Fabrication of scandium stabilized zirconia thin film by electrostatic spray deposition technique for solid oxide fuel cell electrolyte, *Thin Solid Films*, 518 (2010), No. 22, p. 6518.
[24] T. Chalermkiti, M. Panapoy, N. Chaiyut, and B. Ksapabutr, Fabrication of Samarium Doped Ceria Electrolyte on Rough Glass Substrate with High Electrical Conductivity by Electrostatic Spray Deposition for Intermediate Temperature Solid Oxide Fuel Cells, *Energy Procedia*, 34 (2013), p. 471.
[25] I. Taniguchi, R.C. van Landschoot, and J. Schoonman, Fabrication of $La_{1-x}Sr_xCo_{1-y}Fe_yO_3$ thin films by electrostatic spray deposition, *Solid State Ion.*, 156 (2003), No. 1-2, p. 1.
[26] D. Perednis, O. Wilhelm, S.E. Pratsinis, and L.J. Gauckler, Morphology and deposition of thin yttria-stabilized zirconia films using spray pyrolysis, *Thin Solid Films*, 474 (2005), No. 1, p. 84.
[27] T. Schneller, and D. Griesche, Inkjet Printed Y-Substituted Barium Zirconate Layers as Electrolyte Membrane for Thin Film Electrochemical Devices, *Membranes-Basel*, 9 (2019), No. 10, p. 131.
[28] E.Y. Pikalova, and E.G. Kalinina, Place of electrophoretic deposition among thin-film methods adapted to the solid oxide fuel cell technology: A short review, *Int. J. Energy Prod. Manag.*, 4 (2019), No. 1, p. 1.
[29] J. Engels, D. Griesche, R. Waser, and T. Schneller, Thin film proton conducting membranes for micro-solid oxide fuel cells by chemical solution deposition, *Thin Solid Films*, 636 (2017), p. 446.
[30] T. Van Gestel, D. Sebold, and H.P. Buchkremer, Processing of 8YSZ and CGO thin film electrolyte layers for intermediate- and low-temperature SOFCs, *J. Eur. Ceram. Soc.*, 35 (2015), No. 5, p. 1505.

[31] J.H. Park, S.M. Han, K.J. Yoon, H. Kim, J. Hong, B.-K. Kim, J.-H. Lee, and J.-W. Son, Impact of nanostructured anode on low-temperature performance of thin-film-based anode-supported solid oxide fuel cells, *J. Power Sources*, 315 (2016), p. 324.
[32] J.H. Park, S.M. Han, B.-K. Kim, J.-H. Lee, K.J. Yoon, H. Kim, H.-I. Ji, and J.-W. Son, Sintered powder-base cathode over vacuum-deposited thin-film electrolyte of low-temperature solid oxide fuel cell: Performance and stability, *Electrochim. Acta*, 296 (2019), p. 1055.
[33] K. Bae, S. Lee, D.Y. Jang, H.J. Kim, H. Lee, D. Shin, J.-W. Son, and J.H. Shim, High-performance protonic ceramic fuel cells with thin-film yttrium-doped barium cerate–zirconate electrolytes on compositionally gradient anodes, *ACS Appl. Mater. Interfaces*, 8 (2016), No. 14, p. 9097.
[34] H.-S. Noh, K.J. Yoon, B.-K. Kim, H.-J. Je, H.-W. Lee, J.-H. Lee, and J.-W. Son, The potential and challenges of thin-film electrolyte and nanostructured electrode for yttria-stabilized zirconia-base anode-supported solid oxide fuel cells, *J. Power Sources*, 247 (2014), p. 105.
[35] G.Y. Cho, Y.H. Lee, S.W. Hong, J. Bae, J. An, Y.B. Kim, and S.W. Cha, High-performance thin film solid oxide fuel cells with scandia-stabilized zirconia (ScSZ) thin film electrolyte, *Int. J. Hydrogen Energy*, 40 (2015), No. 45, p. 15704.
[36] G.Y. Cho, Y. Kim, S.W. Hong, W. Yu, Y.-B. Kim, and S.W. Cha, Optimization of ScSZ/GDC bilayer thin film electrolyte for anodic aluminum oxide supported low temperature solid oxide fuel cells, *Nanotechnology*, 29 (2018), No. 34, p. 345401.
[37] J. An, Y.-B. Kim, J. Park, T.M. Gür, and F.B. Prinz, Three-dimensional nanostructured bilayer solid oxide fuel cell with 1.3 W/cm^2 at 450 °C, *Nano Lett.*, 13 (2013), No. 9, p. 4551.
[38] Y.H. Lee, I. Chang, G.Y. Cho, J. Park, W. Yu, W.H. Tanveer, and S.W. Cha, Thin film solid oxide fuel cells operating below 600 °C: a review, *Int. J. Precis. Eng. Manuf. - Green Technol.*, 5 (2018), No. 3, p. 441.
[39] M. Tsuchiya, B.-K. Lai, and S. Ramanathan, Scalable nanostructured membranes for solid-oxide fuel cells, *Nature Nanotechnology*, 6 (2011), No. 5, p. 282.
[40] H.-S. Noh, J.-W. Son, H. Lee, H.-I. Ji, J.-H. Lee, and H.-W. Lee, Suppression of Ni agglomeration in PLD fabricated Ni-YSZ composite for surface modification of SOFC anode, *J. Eur. Ceram. Soc.*, 30 (2010), No. 16, p. 3415.
[41] S. Kang, J. Lee, G.Y. Cho, Y. Kim, S. Lee, S.W. Cha, and J. Bae, Scalable fabrication process of thin-film solid oxide fuel cells with an anode functional layer design and a sputtered electrolyte, *Int. J. Hydrogen Energy*, 45 (2020), No. 58, p. 33980.
[42] S. Jo, B. Sharma, D.-H. Park, and J.-h. Myung, Materials and nano-structural processes for use in solid oxide fuel cells: a review, *J. Korean Ceram. Soc.*, (2020), p. 135.
[43] U.P. Muecke, D. Beckel, A. Bernard, A. Bieberle‐Hütter, S. Graf, A. Infortuna, P. Müller, J.L. Rupp, J. Schneider, and L.J. Gauckler, Micro solid oxide fuel cells on glass ceramic substrates, *Adv. Funct. Mater.*, 18 (2008), No. 20, p. 3158.
[44] J. Fleig, H. Tuller, and J. Maier, Electrodes and electrolytes in micro-SOFCs: a discussion of geometrical constraints, *Solid State Ion.*, 174 (2004), No. 1-4, p. 261.
[45] T. Ishihara, H. Eto, and J. Yan, Intermediate temperature solid oxide fuel cells using $LaGaO_3$ based oxide film deposited by PLD method, *Int. J. Hydrogen Energy*, 36 (2011), No. 2, p. 1862.
[46] A. Pandiyan, A. Uthayakumar, R. Subrayan, S.W. Cha, and S.B. Krishna Moorthy, Review of solid oxide electrolysis cells: a clean energy strategy for hydrogen generation, *Nanomater. Nanotechnol.*, 8 (2019), No. 1, p. 2.
[47] S. Wang, X. Hao, and W. Zhan, Research on a low temperature reversible solid oxide cell, *Int. J. Hydrogen Energy*, 42 (2017), No. 50, p. 29881.
[48] C.-A. Thieu, J. Hong, H. Kim, K.J. Yoon, J.-H. Lee, B.-K. Kim, and J.-W. Son, Incorporation of a Pd catalyst at the fuel electrode of a thin-film-based solid oxide cell by multi-layer deposition and its impact on low-temperature co-electrolysis, *J. Mater. Chem. A* . 5 (2017), No. 16, p. 7433.
[49] H. Shimada, T. Yamaguchi, H. Kishimoto, H. Sumi, Y. Yamaguchi, K. Nomura, and Y. Fujishiro, Nanocomposite electrodes for high current density over 3 A cm^{-2} in solid oxide electrolysis cells, *Nat. Commun.*, 10 (2019), No. 1, p. 5432.

[50] W. Li, B. Guan, L. Ma, H. Tian, and X. Liu, Synergistic Coupling of Proton Conductors $BaZr_{0.1}Ce_{0.7}Y_{0.1}Yb_{0.1}O_{3-\delta}$ and $La_2Ce_2O_7$ to Create Chemical Stable, Interface Active Electrolyte for Steam Electrolysis Cells, *ACS Appl. Mater. Interfaces*, 11 (2019), No. 20, p. 18323.

[51] L. Bernadet, C. Moncasi, M. Torrell, and A. Tarancón, High-performing electrolyte-supported symmetrical solid oxide electrolysis cells operating under steam electrolysis and co-electrolysis modes, *Int. J. Hydrogen Energy*, 45 (2020), No. 28, p. 14208.

[52] M.Z. Khan, R.-H. Song, M.T. Mehran, S.-B. Lee, and T.-H. Lim, Controlling cation migration and inter-diffusion across cathode/interlayer/electrolyte interfaces of solid oxide fuel cells: A review, *Ceram. Int.*, 47 (2021), No. 5, p. 5839.

[53] S.R. Phadke, C.R. Bowers, E.D. Wachsman, and J.C. Nino, Proton conduction in acceptor doped SnP_2O_7, *Solid State Ion.*, 183 (2011), No. 1, p. 26.

[54] A. Lapina, C. Chatzichristodoulou, J. Hallinder, P. Holtappels, and M. Mogensen, Electrical conductivity of titanium pyrophosphate between 100 and 400 °C: effect of sintering temperature and phosphorus content, *J. Solid State Electrochem.*, 18 (2014), No. 1, p. 39.

[55] L.S. Wang, and S.A. Barnett, Ag-perovskite cermets for thin film solid oxide fuel cell air-electrode applications, *Solid State Ion.*, 76 (1995), No. 1, p. 103.

[56] J.L. Hertz, and H.L. Tuller, Nanocomposite Platinum–Yttria Stabilized Zirconia Electrode and Implications for Micro-SOFC Operation, *J. Electrochem. Soc.*, 154 (2007), No. 4, p. B413.

[57] F.J. Garcia-Garcia, F. Yubero, A.R. González-Elipe, S.P. Balomenou, D. Tsiplakides, I. Petrakopoulou, and R.M. Lambert, Porous, robust highly conducting Ni-YSZ thin film anodes prepared by magnetron sputtering at oblique angles for application as anodes and buffer layers in solid oxide fuel cells, *Int. J. Hydrogen Energy*, 40 (2015), No. 23, p. 7382.

[58] J.H. Park, J.-H. Lee, K.J. Yoon, H. Kim, H.-I. Ji, S. Yang, S. Park, S.M. Han, and J.-W. Son, A nanoarchitectured cermet composite with extremely low Ni content for stable high-performance solid oxide fuel cells, *Acta Mater.*, 206 (2021), p. 116580.

[59] T.M. Onn, R. Küngas, P. Fornasiero, K. Huang, and R.J. Gorte, Atomic Layer Deposition on Porous Materials: Problems with Conventional Approaches to Catalyst and Fuel Cell Electrode Preparation, *Inorganics*, 6 (2018), No. 1, p. 34.

[60] S. Oh, S. Hong, H.J. Kim, Y.-B. Kim, and J. An, Enhancing thermal-stability of metal electrodes with a sputtered gadolinia-doped ceria over-layer for low-temperature solid oxide fuel cells, *Ceram. Int.*, 43 (2017), No. 7, p. 5781.

[61] J. Zhou, T.-H. Shin, C. Ni, G. Chen, K. Wu, Y. Cheng, and J.T.S. Irvine, In situ growth of nanoparticles in layered perovskite $La_{0.8}Sr_{1.2}Fe_{0.9}Co_{0.1}O_{4-\delta}$ as an active and stable electrode for symmetrical solid oxide fuel cells, *Chem Mater*, 28 (2016), No. 9, p. 2981.

[62] J. Zhou, J. Yang, Z. Zong, L. Fu, Z. Lian, C. Ni, J. Wang, Y. Wan, and K. Wu, A mesoporous catalytic fiber architecture decorated by exsolved nanoparticles for reversible solid oxide cells, *J. Power Sources*, 468 (2020), p. 228349.

[63] J. Li, W. Xie, S. Zhang, S.-M. Xu, and M. Shao, Boosting the rate performance of Li–S batteries under high mass-loading of sulfur based on a hierarchical NCNT@Co-CoP nanowire integrated electrode, *J. Mater. Chem. A* . 9 (2021), No. 18, p. 11151.

[64] S.Y. Lim, S. Martin, G. Gao, Y. Dou, S.B. Simonsen, J.O. Jensen, Q. Li, K. Norrman, S. Jing, and W. Zhang, Self-Standing Nanofiber Electrodes with Pt–Co Derived from Electrospun Zeolitic Imidazolate Framework for High Temperature PEM Fuel Cells, *Adv. Funct. Mater.*, 31 (2021), No. 7, p. 2006771.

[65] J. Gong, P. Wu, Z. Bai, J. Ma, T. Li, Y. Yao, and C. Jiang, Insight into the Electrospinning Process for SOFC Cathode Nanofibers, *J. Phys. Chem. C*, 125 (2021), No. 13, p. 7044.

[66] X. Zhang, J. Li, L. Wang, X. Guo, H. Sun, H. Zhang, and Q. Hu, Improved electrochemical performance of Bi doped $La_{0.8}Sr_{0.2}FeO_{3-\delta}$ nanofiber cathode for IT-SOFCs via electrospinning, *Ceram. Int.*, 47 (2021), No. 1, p. 534.

[67] J. Parbey, M. Xu, J. Lei, M. Espinoza-Andaluz, T.S. Li, and M. Andersson, Electrospun fabrication of nanofibers as high-performance cathodes of solid oxide fuel cells, *Ceram. Int.*, 46 (2020), No. 5, p. 6969.
[68] Y. Zhang, F. Yan, M. Yan, Y. Wan, Z. Jiao, C. Xia, F. Chen, and M. Ni, High-throughput, super-resolution 3D reconstruction of nano-structured solid oxide fuel cell electrodes and quantification of microstructure-property relationships, *J. Power Sources*, 427 (2019), p. 112.
[69] J. Chen, X. Wang, P. Boldrin, N.P. Brandon, and A. Atkinson, Hierarchical dual-porosity nanoscale nickel cermet electrode with high performance and stability, *Nanoscale*, 11 (2019), No. 38, p. 17746.
[70] M. Ouyang, A. Bertei, S.J. Cooper, Y. Wu, P. Boldrin, X. Liu, M. Kishimoto, H. Wang, M.N. Marlow, and J. Chen, Model-guided design of a high performance and durability Ni nanofiber/ceria matrix solid oxide fuel cell electrode, *J. Energy Chem.*, 56 (2021), p. 98.
[71] J.M. Vohs, and R.J. Gorte, High-Performance SOFC Cathodes Prepared by Infiltration, *Adv. Mater.*, 21 (2009), No. 9, p. 943.
[72] B. Hua, N. Yan, M. Li, Y.-F. Sun, Y.-Q. Zhang, J. Li, T. Etsell, P. Sarkar, and J.-L. Luo, Anode-Engineered Protonic Ceramic Fuel Cell with Excellent Performance and Fuel Compatibility, *Adv. Mater.*, 28 (2016), No. 40, p. 8922.
[73] Y. Liu, S. Zha, and M. Liu, Novel Nanostructured Electrodes for Solid Oxide Fuel Cells Fabricated by Combustion Chemical Vapor Deposition (CVD), *Adv. Mater.*, 16 (2004), No. 3, p. 256.
[74] P. Boldrin, E. Ruiz-Trejo, J. Mermelstein, J.M. Bermúdez Menéndez, T. Ramírez Reina, and N.P. Brandon, Strategies for Carbon and Sulfur Tolerant Solid Oxide Fuel Cell Materials, Incorporating Lessons from Heterogeneous Catalysis, *Chem. Rev.*, 116 (2016), No. 22, p. 13633.
[75] L. Bian, C. Duan, L. Wang, Z. Chen, Y. Hou, J. Peng, X. Song, S. An, and R. O'Hayre, An all-oxide electrolysis cells for syngas production with tunable H_2/CO yield via co-electrolysis of H_2O and CO_2, *J. Power Sources*, 482 (2021), p. 228887.
[76] D. Ding, X. Li, S.Y. Lai, K. Gerdes, and M. Liu, Enhancing SOFC cathode performance by surface modification through infiltration, *Energy Environ. Sci.*, 7 (2014), No. 2, p. 552.
[77] K.-Y. Liu, L. Fan, C.-C. Yu, and P.-C. Su, Thermal stability and performance enhancement of nano-porous platinum cathode in solid oxide fuel cells by nanoscale ZrO_2 capping, *Electrochem. Commun.*, 56 (2015), p. 65.
[78] I. Chang, S. Ji, J. Park, M.H. Lee, and S.W. Cha, Ultrathin YSZ coating on Pt cathode for high thermal stability and enhanced oxygen reduction reaction activity, *Adv. Energy Mater.*, 5 (2015), No. 10, p. 1402251.
[79] A. Karimaghaloo, A.M. Andrade, S. Grewal, J.H. Shim, and M.H. Lee, Mechanism of cathodic performance enhancement by a few-nanometer-thick oxide overcoat on porous Pt cathodes of solid oxide fuel cells, *ACS Omega*, 2 (2017), No. 3, p. 806.
[80] K.D. Kreuer, Proton-Conducting Oxides, *Annu. Rev. Mater. Res.*, 33 (2003), No. 1, p. 333.
[81] H. Iwahara, T. Esaka, H. Uchida, and N. Maeda, Proton Conduction in Sintered Oxides and Its Application to Steam Electrolysis for Hydrogen-Production, *Solid State Ion.*, 3-4 (1981), No. Aug, p. 359.
[82] H. Iwahara, H. Uchida, and I. Yamasaki, High-Temperature Steam Electrolysis Using Srceo3-Based Proton Conductive Solid Electrolyte, *Int. J. Hydrogen Energy*, 12 (1987), No. 2, p. 73.
[83] H. Iwahara, H. Uchida, and N. Maeda, Studies on Solid Electrolyte Gas Cells with High-Temperature-Type Proton Conductor and Oxide Ion Conductor, *Solid State Ion.*, 11 (1983), No. 2, p. 109.
[84] H. Iwahara, H. Uchida, K. Ono, and K. Ogaki, Proton Conduction in Sintered Oxides Based on $BaCeO_3$, *J. Electrochem. Soc.*, 135 (1988), No. 2, p. 529.
[85] T. Norby, Solid-state protonic conductors: principles, properties, progress and prospects, *Solid State Ion.*, 125 (1999), No. 1-4, p. 1.
[86] Y.Q. Meng, J. Gao, Z.Y. Zhao, J. Amoroso, J.H. Tong, and K.S. Brinkman, Review: recent progress in low-temperature proton-conducting ceramics, *J. Mater. Sci.*, 54 (2019), No. 13, p. 9291.

[87] O. Paschos, J. Kunze, U. Stimming, and F. Maglia, A review on phosphate based, solid state, protonic conductors for intermediate temperature fuel cells, *J. Phys.-Condens. Mat.*, 23 (2011), No. 23, p. 234110.
[88] I.A. Stenina, and A.B. Yaroslavtsev, Low- and intermediate-temperature proton-conducting electrolytes, *Inorg. Mater.*, 53 (2017), No. 3, p. 253.
[89] J. Kim, S. Sengodan, S. Kim, O. Kwon, Y. Bu, and G. Kim, Proton conducting oxides: A review of materials and applications for renewable energy conversion and storage, *Renew. Sust. Energ. Rev.*, 109 (2019), p. 606.
[90] S. Hossain, A.M. Abdalla, S.N.B. Jamain, J.H. Zaini, and A.K. Azad, A review on proton conducting electrolytes for clean energy and intermediate temperature-solid oxide fuel cells, *Renew. Sust. Energ. Rev.*, 79 (2017), p. 750.
[91] H. Takahashi, I. Yashima, K. Amezawa, K. Eguchi, H. Matsumoto, H. Takamura, and S. Yamaguchi, First-Principles Calculations for the Energetics of the Hydration Reaction of Acceptor-Doped BaZrO3, *Chem. Mater.*, 29 (2017), No. 4, p. 1518.
[92] C. Kjølseth, L.-Y. Wang, R. Haugsrud, and T. Norby, Determination of the enthalpy of hydration of oxygen vacancies in Y-doped $BaZrO_3$ and $BaCeO_3$ by TG-DSC, *Solid State Ion.*, 181 (2010), No. 39-40, p. 1740.
[93] Y. Jing, and N.R. Aluru, The role of A-site ion on proton diffusion in perovskite oxides (ABO3), *J. Power Sources*, 445 (2020), p. 227327.
[94] S.J. Stokes, and M.S. Islam, Defect chemistry and proton-dopant association in $BaZrO_3$ and $BaPrO_3$, *J. Mater. Chem.*, 20 (2010), No. 30, p. 6258.
[95] J.A. Dawson, and I. Tanaka, Proton incorporation and trapping in ZrO_2 grain boundaries, *J. Mater. Chem. A*, 2 (2014), No. 5, p. 1400.
[96] J.A. Dawson, H. Chen, and I. Tanaka, Protonic defects in yttria stabilized zirconia: incorporation, trapping and migration, *Phys. Chem. Chem. Phys.*, 16 (2014), No. 10, p. 4814.
[97] Y. Yamazaki, F. Blanc, Y. Okuyama, L. Buannic, J.C. Lucio-Vega, C.P. Grey, and S.M. Haile, Proton trapping in yttrium-doped barium zirconate, *Nat. Mater.*, 12 (2013), No. 7, p. 647.
[98] C. Karmonik, T.J. Udovic, R.L. Paul, J.J. Rush, K. Lind, and R. Hempelmann, Observation of dopant effects on hydrogen modes in $SrCe_{0.95}M_{0.05}H_xO_{3-\delta}$ by neutron vibrational spectroscopy, *Solid State Ion.*, 109 (1998), No. 3-4, p. 207.
[99] R. Hempelmann, M. Soetratmo, O. Hartmann, and R. Wappling, Muon diffusion and trapping in proton conducting oxides, *Solid State Ion.*, 107 (1998), No. 3-4, p. 269.
[100] H.S. Kim, A. Jang, S.Y. Choi, W. Jung, and S.Y. Chung, Vacancy-induced electronic structure variation of acceptors and correlation with proton conduction in perovskite oxides, *Angew. Chem. Int. Ed.*, 55 (2016), No. 43, p. 13499.
[101] I. Oikawa, and H. Takamura, Correlation among Oxygen Vacancies, Protonic Defects, and the Acceptor Dopant in Sc-Doped $BaZrO_3$ Studied by 45Sc Nuclear Magnetic Resonance, *Chem. Mater.*, 27 (2015), No. 19, p. 6660.
[102] S. Wang, J. Shen, Z. Zhu, Z. Wang, Y. Cao, X. Guan, Y. Wang, Z. Wei, and M. Chen, Further optimization of barium cerate properties via co-doping strategy for potential application as proton-conducting solid oxide fuel cell electrolyte, *J. Power Sources*, 387 (2018), p. 24.
[103] J. LÜ, L. Wang, L. Fan, Y. Li, L. Dai, and H. Guo, Chemical stability of doped $BaCeO_3$-$BaZrO_3$ solid solutions in different atmospheres, *J. Rare Earths*, 26 (2008), No. 4, p. 505.
[104] J.-H. Kim, Y.-M. Kang, M.-S. Byun, and K.-T. Hwang, Study on the chemical stability of Y-doped $BaCeO_{3-\delta}$ and $BaZrO_{3-\delta}$ films deposited by aerosol deposition, *Thin Solid Films*, 520 (2011), No. 3, p. 1015.
[105] K. Katahira, Y. Kohchi, T. Shimura, and H. Iwahara, Protonic conduction in Zr-substituted $BaCeO_3$, *Solid State Ion.*, 138 (2000), No. 1-2, p. 91.
[106] D. Pergolesi, E. Fabbri, A. D'Epifanio, E. Di Bartolomeo, A. Tebano, S. Sanna, S. Licoccia, G. Balestrino, and E. Traversa, High proton conduction in grain-boundary-free yttrium-doped barium zirconate films grown by pulsed laser deposition, *Nat. Mater.*, 9 (2010), No. 10, p. 846.

[107] Z. Zhu, S. Wang, J. Shen, X. Meng, Y. Cao, Z. Wang, and Z. Wei, Effect of low-level Ca_{2+} substitution at perovskite B site on the properties of $BaZr_{0.8}Y_{0.2}O_{3-\delta}$, *J. Alloys Compd.*, 805 (2019), p. 718.
[108] F. Iguchi, T. Tsurui, N. Sata, Y. Nagao, and H. Yugami, The relationship between chemical composition distributions and specific grain boundary conductivity in Y-doped $BaZrO_3$ proton conductors, *Solid State Ion.*, 180 (2009), No. 6-8, p. 563.
[109] F. Iguchi, N. Sata, T. Tsurui, and H. Yugami, Microstructures and grain boundary conductivity of $BaZr_{1-x}Y_xO_3$ (x=0.05, 0.10, 0.15) ceramics, *Solid State Ion.*, 178 (2007), No. 7-10, p. 691.
[110] C. Zuo, S. Zha, M. Liu, M. Hatano, and M. Uchiyama, $Ba(Zr_{0.1}Ce_{0.7}Y_{0.2})O_{3-\delta}$ as an Electrolyte for Low-Temperature Solid-Oxide Fuel Cells, *Adv. Mater.*, 18 (2006), No. 24, p. 3318.
[111] J. Yin, X. Wang, J. Xu, H. Wang, F. Zhang, and G. Ma, Ionic conduction in $BaCe_{0.85-x}Zr_xEr_{0.15}O_{3-\alpha}$ and its application to ammonia synthesis at atmospheric pressure, *Solid State Ion.*, 185 (2011), No. 1, p. 6.
[112] M. Hakim, C.-Y. Yoo, J.H. Joo, and J.H. Yu, Enhanced durability of a proton conducting oxide fuel cell with a purified yttrium-doped barium zirconate-cerate electrolyte, *J. Power Sources*, 278 (2015), p. 320.
[113] S. Yang, Y. Wen, S. Zhang, S. Gu, Z. Wen, and X. Ye, Performance and stability of $BaCe_{0.8-x}Zr_{0.2}In_xO_{3-\delta}$-based materials and reversible solid oxide cells working at intermediate temperature, *Int. J. Hydrogen Energy*, 42 (2017), No. 47, p. 28549.
[114] E. Bevillon, G. Dezanneau, and G. Geneste, Oxygen incorporation in acceptor-doped perovskites, *Phys. Rev. B*, 83 (2011), No. 17, p. 174101.
[115] L. He, F. Zhang, Y. Xuan, L. Zhang, H. Gao, H. Pan, S. Lian, M. Wang, J. Yin, X. Chen, J. Ren, and M. Chen, Unveiling The Effect of Dopants on the Hydration Reaction and Proton Conduction of Nd and Y Co-Doped $BaZrO_3$ in Solid Oxide Fuel Cells, *J. Electrochem. Soc.*, 168 (2021), No. 3, p.
[116] M.D. Goncalves, P.S. Maram, R. Muccillo, and A. Navrotsky, Enthalpy of formation and thermodynamic insights into yttrium doped $BaZrO_3$, *J. Mater. Chem. A* . 2 (2014), No. 42, p. 17840.
[117] K.D. Kreuer, S. Adams, W. Munch, A. Fuchs, U. Klock, and J. Maier, Proton conducting alkaline earth zirconates and titanates for high drain electrochemical applications, *Solid State Ion.*, 145 (2001), No. 1-4, p. 295.
[118] T. Schober, and H.G. Bohn, Water vapor solubility and electrochemical characterization of the high temperature proton conductor $BaZr_{0.9}Y_{0.1}O_{2.95}$, *Solid State Ion.*, 127 (2000), No. 3-4, p. 351.
[119] K.D. Kreuer, Aspects of the formation and mobility of protonic charge carriers and the stability of perovskite-type oxides, *Solid State Ion.*, 125 (1999), No. 1-4, p. 285.
[120] D. Tsvetkov, I. Ivanov, D. Malyshkin, V. Sereda, and A. Zuev, Thermoelectric Behavior of $BaZr_{0.9}Y_{0.1}O_{3-\delta}$ Proton Conducting Electrolyte, *Membranes*, 9 (2019), No. 9, p. 120.
[121] S. Ricote, N. Bonanos, and G. Caboche, Water vapour solubility and conductivity study of the proton conductor $BaCe_{(0.9-x)}Zr_xY_{0.1}O_{(3-\delta)}$, *Solid State Ion.*, 180 (2009), No. 14-16, p. 990.
[122] H. Zhu, S. Ricote, C. Duan, R.P. O'Hayre, D.S. Tsvetkov, and R.J. Kee, Defect Incorporation and Transport within Dense $BaZr_{0.8}Y_{0.2}O_{3-\delta}$ (BZY20) Proton-Conducting Membranes, *J Electrochem Soc*, 165 (2018), No. 9, p. F581.
[123] Y. Yamazaki, P. Babilo, and S.M. Haile, Defect Chemistry of Yttrium-Doped Barium Zirconate: A Thermodynamic Analysis of Water Uptake, *Chem. Mater.*, 20 (2008), No. 20, p. 6352.
[124] F. Giannici, A. Longo, A. Balerna, K.D. Kreuer, and A. Martorana, Proton Dynamics in In:$BaZrO_3$: Insights on the Atomic and Electronic Structure from X-ray Absorption Spectroscopy, *Chem. Mater.*, 21 (2009), No. 13, p. 2641.
[125] A. Løken, T.S. Bjørheim, and R. Haugsrud, The pivotal role of the dopant choice on the thermodynamics of hydration and associations in proton conducting $BaCe_{0.9}X_{0.1}O_{3-\delta}$ (X = Sc, Ga, Y, In, Gd and Er), *J. Mater. Chem. A* . 3 (2015), No. 46, p. 23289.
[126] H. Zhu, S. Ricote, C. Duan, R.P. O'Hayre, and R.J. Kee, Defect Chemistry and Transport within Dense $BaCe_{0.7}Zr_{0.1}Y_{0.1}Yb_{0.1}O_{3-\delta}$ (BCZYYb) Proton-Conducting Membranes, *J. Electrochem. Soc.*, 165 (2018), No. 10, p. F845.

[127] H.G. Bohn, and T. Schober, Electrical conductivity of the high-temperature proton conductor $BaZr_{0.9}Y_{0.1}O_{2.95}$, *J. Am. Ceram. Soc.*, 83 (2000), No. 4, p. 768.
[128] M.E. Bjorketun, P.G. Sundell, and G. Wahnstrom, Effect of acceptor dopants on the proton mobility in $BaZrO_3$: A density functional investigation, *Phys. Rev. B*, 76 (2007), No. 5, p. 054307.
[129] B. Merinov, and W.A. Goddard, Proton diffusion pathways and rates in Y-doped $BaZrO_3$ solid oxide electrolyte from quantum mechanics, *J. Chem. Phys.*, 130 (2009), No. 19, p. 194707.
[130] D.Z. Sahraoui, and T. Mineva, Effect of dopant nature on structures and lattice dynamics of proton-conducting $BaZrO_3$, *Solid State Ion.*, 253 (2013), p. 195.
[131] X. Yang, L. Jia, B. Pan, B. Chi, J. Pu, and J. Li, Mechanism of Proton Conduction in Doped Barium Cerates: A First-Principles Study, *J. Phys. Chem. C*, 124 (2020), No. 14, p. 8024.
[132] J. Ding, J. Balachandran, X. Sang, W. Guo, J.S. Anchell, G.M. Veith, C.A. Bridges, Y. Cheng, C.M. Rouleau, J.D. Poplawsky, N. Bassiri-Gharb, R.R. Unocic, and P. Ganesh, The Influence of Local Distortions on Proton Mobility in Acceptor Doped Perovskites, *Chem. Mater.*, 30 (2018), No. 15, p. 4919.
[133] E. Gilardi, E. Fabbri, L. Bi, J.L.M. Rupp, T. Lippert, D. Pergolesi, and E. Traversa, Effect of dopant-host ionic radii mismatch on acceptor-doped barium zirconate microstructure and proton conductivity, *J Phys Chem C*, 121 (2017), No. 18, p. 9739.
[134] G. Accardo, D. Frattini, and S.P. Yoon, Enhanced proton conductivity of Gd–Co bi-doped barium cerate perovskites based on structural and microstructural investigations, *J. Alloys Compd.*, 834 (2020), p. 155114.
[135] A. Radojković, M. Žunić, S.M. Savić, S. Perać, D.L. Golić, Z. Branković, and G. Branković, Co-doping as a strategy for tailoring the electrolyte properties of $BaCe_{0.9}Y_{0.1}O_{3-\delta}$, *Ceram. Int.*, 45 (2019), No. 7, p. 8279.
[136] L.I. Holz, V.C. Graça, F.J. Loureiro, and D.P. Fagg, *Analysis of the Electrochemical Transport Properties of Doped Barium Cerate for Proton Conductivity in Low Humidity Conditions: A Review*, Analytical Chemistry-Advancement, Perspectives and Applications, IntechOpen, London, 2020.
[137] J.L. Yin, X.W. Wang, J.H. Xu, H.T. Wang, F. Zhang and G.L. Ma, Ionic conduction in BaCe0.85-xZrxEr0.15O3-alpha and its application to ammonia synthesis at atmospheric pressure, *Solid State Ionics* 185 (2011), No. 1, p. 6.
[138] W. Sun, M. Liu, and W. Liu, Chemically Stable Yttrium and Tin Co-Doped Barium Zirconate Electrolyte for Next Generation High Performance Proton-Conducting Solid Oxide Fuel Cells, *Adv. Energy Mater.*, 3 (2013), No. 8, p. 1041.
[139] A. Satapathy, and E. Sinha, A comparative proton conductivity study on Yb-doped $BaZrO_3$ perovskite at intermediate temperatures under wet N_2 environment, *J. Alloys Compd.*, 772 (2019), p. 675.
[140] A. Satapathy, E. Sinha, and S.K. Rout, Investigation of proton conductivity in Sc and Yb co-doped barium zirconate ceramics, *Mater. Res. Express*, 6 (2019), No. 5, p. 056305.
[141] Y. Meng, J. Gao, H. Huang, M. Zou, J. Duffy, J. Tong, and K.S. Brinkman, A high-performance reversible protonic ceramic electrochemical cell based on a novel Sm-doped $BaCe_{0.7}Zr_{0.1}Y_{0.2}O_{3-\delta}$ electrolyte, *J. Power Sources*, 439 (2019), p. 227093.
[142] S. Rajendran, N.K. Thangavel, S. Alkatie, Y. Ding, and L.M.R. Arava, Y, Gd, and Pr tri-doped perovskite-type proton conducting electrolytes with improved sinterability and chemical stability, *J. Alloys Compd.*, 870 (2021), p. 159431.
[143] F. He, Q. Gao, Z. Liu, M. Yang, R. Ran, G. Yang, W. Wang, W. Zhou, and Z. Shao, A New Pd Doped Proton Conducting Perovskite Oxide with Multiple Functionalities for Efficient and Stable Power Generation from Ammonia at Reduced Temperatures, *Adv. Energy Mater.*, 11 (2021), No. 19, p. 2003916.
[144] C.S. Tu, R.R. Chien, V.H. Schmidt, S.C. Lee, C.C. Huang, and C.L. Tsai, Thermal stability of $Ba(Zr_{0.8-x}Ce_xY_{0.2})O_{2.9}$ ceramics in carbon dioxide, *J. Appl. Phys.*, 105 (2009), No. 10, p.

[145] P. Babilo, and S.M. Haile, Enhanced sintering of yttrium-doped barium zirconate by addition of ZnO, *J. Am. Ceram. Soc.*, 88 (2005), No. 9, p. 2362.
[146] S.W. Tao, and J.T.S. Irvine, A stable, easily sintered proton-conducting oxide electrolyte for moderate-temperature fuel cells and electrolyzers, *Adv. Mater.*, 18 (2006), No. 12, p. 1581.
[147] E. Fabbri, L. Bi, H. Tanaka, D. Pergolesi, and E. Traversa, Chemically Stable Pr and Y Co-Doped Barium Zirconate Electrolytes with High Proton Conductivity for Intermediate-Temperature Solid Oxide Fuel Cells, *Adv. Funct. Mater.*, 21 (2011), No. 1, p. 158.
[148] W.P. Sun, Z.W. Zhu, Z. Shi, and W. Liu, Chemically stable and easily sintered high-temperature proton conductor $BaZr_{0.8}In_{0.2}O_{3-\delta}$ for solid oxide fuel cells, *J. Power Sources*, 229 (2013), p. 95.
[149] Z.M. Zhong, Stability and conductivity study of the $BaCe_{0.9-x}Zr_xY_{0.1}O_{2.95}$ systems, *Solid State Ion.*, 178 (2007), No. 3-4, p. 213.
[150] K.H. Ryu, and S.M. Haile, Chemical stability and proton conductivity of doped $BaCeO_3$-$BaZrO_3$ solid solutions, *Solid State Ion.*, 125 (1999), No. 1-4, p. 355.
[151] D.A. Medvedev, E.V. Gorbova, A.K. Demin, and B.D. Antonov, Structure and electric properties of $BaCe_{0.77-x}Zr_xGd_{0.2}Cu_{0.03}O_{3-\delta}$, *Russ. J. Electrochem.*, 47 (2011), No. 12, p. 1404.
[152] S.J. Zhan, X.F. Zhu, W.P. Wang, and W.S. Yang, Stability and transport conductivity of Perovskite type $BaZr_xCe_{0.8-x}Nd_{0.2}O_{3-\delta}$, *Adv. Mater. Res.*, 554 (2012), p. 404.
[153] F.L. Chen, O.T. Sorensen, G.Y. Meng, and D.K. Peng, Chemical stability study of $BaCe_{0.9}Nd_{0.1}O_3$-alpha high-temperature proton-conducting ceramic, *J Mater Chem*, 7 (1997), No. 3, p. 481.
[154] H. Matsumoto, Y. Kawasaki, N. Ito, M. Enoki, and T. Ishihara, Relation Between Electrical Conductivity and Chemical Stability of $BaCeO_3$-Based Proton Conductors with Different Trivalent Dopants, *Electrochem. Solid-State Lett.*, 10 (2007), No. 4, p B77.
[155] Y.-P. Fu, and C.-S. Weng, Effect of rare-earth ions doped in $BaCeO_3$ on chemical stability, mechanical properties, and conductivity properties, *Ceram. Int.*, 40 (2014), No. 7, p. 10793.
[156] G.S. Reddy, and R. Bauri, Y and In-doped $BaCeO_3$-$BaZrO_3$ solid solutions: Chemically stable and easily sinterable proton conducting oxides, *J. Alloys Compd.*, 688 (2016), p. 1039.
[157] S.V. Bhide, and A.V. Virkar, Stability of $BaCeO_3$-based proton conductors in water-containing atmospheres, *J. Electrochem. Soc.*, 146 (1999), No. 6, p. 2038.
[158] S. Rajendran, N.K. Thangavel, H. Ding, Y. Ding, D. Ding, and L.M. Reddy Arava, Tri-doped $BaCeO_3$-$BaZrO_3$ as a chemically stable electrolyte with high proton-conductivity for intermediate temperature solid oxide electrolysis cells (SOECs), *ACS Appl. Mater. Interfaces*, 12 (2020), No. 34, p. 38275.
[159] P. Sawant, S. Varma, B.N. Wani, and S.R. Bharadwaj, Synthesis, stability and conductivity of $BaCe_{0.8-x}Zr_xY_{0.2}O_{3-\delta}$ as electrolyte for proton conducting SOFC, *Int. J. Hydrogen Energy*, 37 (2012), No. 4, p. 3848.
[160] A. Radojković, M. Žunić, S.M. Savić, G. Branković, and Z. Branković, Enhanced stability in CO2 of Ta doped $BaCe_{0.9}Y_{0.1}O_{3-\delta}$ electrolyte for intermediate temperature SOFCs, *Ceram. Int.*, 39 (2013), No. 3, p. 2631.
[161] L. Bi, S. Zhang, S. Fang, Z. Tao, R. Peng, and W. Liu, A novel anode supported $BaCe_{0.7}Ta_{0.1}Y_{0.2}O_{3-\delta}$ electrolyte membrane for proton-conducting solid oxide fuel cell, *Electrochem. Commun.*, 10 (2008), No. 10, p. 1598.
[162] J. Dang, Z. Zhu, J. Qian, and W. Liu, A stable $BaCe_{0.7}Ta_{0.1}In_{0.2}O_{3-\delta}$ electrolyte membrane for proton-conducting solid oxide fuel cells, *Ceram. Int.*, 39 (2013), No. 4, p. 4287.
[163] Z. Zhang, L. Chen, Q. Li, T. Song, J. Su, B. Cai, and H. He, High performance In, Ta and Y-doped $BaCeO_3$ electrolyte membrane for proton-conducting solid oxide fuel cells, *Solid State Ion.*, 323 (2018), p. 25.
[164] I.A. Zvonareva, L.R. Tarutina, G.K. Vdovin, J.G. Lyagaeva, A.R. Akhmadeev, and D.A. Medvedev, Heavily Sn-doped barium cerates $BaCe_{0.8-x}Sn_xYb_{0.2}O_{3-\delta}$: Correlations between composition and ionic transport, *Ceram. Int.Ceram. Int.*, 47 (2021), No. 18, p. 26391.

[165] M. Shirpour, R. Merkle, C.T. Lin, and J. Maier, Nonlinear electrical grain boundary properties in proton conducting Y-$BaZrO_3$ supporting the space charge depletion model, *Phys. Chem. Chem. Phys.*, 14 (2012), No. 2, p. 730.
[166] M. Shirpour, R. Merkle, and J. Maier, Space charge depletion in grain boundaries of $BaZrO_3$ proton conductors, *Solid State Ion.*, 225 (2012), p. 304.
[167] A. Lindman, E.E. Helgee, and G. Wahnström, Comparison of Space-Charge Formation at Grain Boundaries in Proton-Conducting $BaZrO_3$ and $BaCeO_3$, *Chem. Mater.*, 29 (2017), No. 18, p. 7931.
[168] M. Vollman, and R. Waser, Grain-Boundary Defect Chemistry of Acceptor-Doped Titanates - Space-Charge Layer Width, *J. Am. Ceram. Soc.*, 77 (1994), No. 1, p. 235.
[169] M. Shirpour, B. Rahmati, W. Sigle, P.A. van Aken, R. Merkle, and J. Maier, Dopant Segregation and Space Charge Effects in Proton-Conducting $BaZrO_3$ Perovskites, *J. Phys. Chem. C*, 116 (2012), No. 3, p. 2453.
[170] D. Medvedev, A. Murashkina, E. Pikalova, A. Demin, A. Podias, and P. Tsiakaras, $BaCeO_3$: Materials development, properties and application, *Prog. Mater Sci.*, 60 (2014), p. 72.
[171] L. Bi, and E. Traversa, Synthesis strategies for improving the performance of doped-$BaZrO_3$ materials in solid oxide fuel cell applications, *J. Mater. Res.*, 29 (2013), No. 1, p. 1.
[172] F.J.A. Loureiro, N. Nasani, G.S. Reddy, N.R. Munirathnam, and D.P. Fagg, A review on sintering technology of proton conducting $BaCeO_3$-$BaZrO_3$ perovskite oxide materials for Protonic Ceramic Fuel Cells, *J. Power Sources*, 438 (2019), p. 226991.
[173] N. Ito, H. Matsumoto, Y. Kawasaki, S. Okada, and T. Ishihara, Introduction of In or Ga as second dopant to $BaZr_{0.9}Y_{0.1}O_{3-\delta}$ to achieve better sinterability, *Solid State Ion.*, 179 (2008), No. 9-10, p. 324.
[174] D. Yun, J. Kim, S.-J. Kim, J.-H. Lee, J.-N. Kim, H. Yoon, J. Yu, M. Kwak, H. Yoon, Y. Cho, and C.-Y. Yoo, Structural and Electrochemical Properties of Dense Yttria-Doped Barium Zirconate Prepared by Solid-State Reactive Sintering, *Energies*, 11 (2018), No. 11, p. 3083.
[175] S. Imashuku, T. Uda, Y. Nose, and Y. Awakura, Fabrication and electrical characterization of 15% yttrium-doped barium zirconate—nitrate freeze drying method combined with vacuum heating, *J. Alloys Compd.*, 509 (2011), No. 9, p. 3872.
[176] D. Han, S. Uemura, C. Hiraiwa, M. Majima, and T. Uda, Detrimental Effect of Sintering Additives on Conducting Ceramics: Yttrium-Doped Barium Zirconate, *ChemSusChem*, 11 (2018), No. 23, p. 4102.
[177] C. Peng, J. Melnik, J.-L. Luo, A.R. Sanger, and K.T. Chuang, $BaZr_{0.8}Y_{0.2}O_{3-\delta}$ electrolyte with and without ZnO sintering aid: Preparation and characterization, *Solid State Ion.*, 181 (2010), No. 29-30, p. 1372.
[178] C. Peng, J. Melnik, J. Li, J. Luo, A.R. Sanger, and K.T. Chuang, ZnO-doped $BaZr_{0.85}Y_{0.15}O_{3-\delta}$ proton-conducting electrolytes: Characterization and fabrication of thin films, *J. Power Sources*, 190 (2009), No. 2, p. 447.
[179] S. Tao, and J.T.S. Irvine, Conductivity studies of dense yttrium-doped $BaZrO_3$ sintered at 1325°C, *J. Solid State Chem.*, 180 (2007), No. 12, p. 3493.
[180] Z. Sun, E. Fabbri, L. Bi, E. Traversa, and R. Koc, Electrochemical Properties and Intermediate-Temperature Fuel Cell Performance of Dense Yttrium-Doped Barium Zirconate with Calcium Addition, *J. Am. Ceram. Soc.*, 95 (2012), No. 2, p. 627.
[181] Z. Sun, E. Fabbri, L. Bi, and E. Traversa, Lowering grain boundary resistance of $BaZr_{0.8}Y_{0.2}O_{3-\delta}$ with $LiNO_3$ sintering-aid improves proton conductivity for fuel cell operation, *Phys. Chem. Chem. Phys.*, 13 (2011), No. 17, p. 7692.
[182] Y. Yamazaki, R. Hernandez-Sanchez, and S.M. Haile, High Total Proton Conductivity in Large-Grained Yttrium-Doped Barium Zirconate, *Chem. Mater.*, 21 (2009), No. 13, p. 2755.
[183] D. Gao, and R. Guo, Structural and electrochemical properties of yttrium-doped barium zirconate by addition of CuO, *J. Alloys Compd.*, 493 (2010), No. 1-2, p. 288.

[184] J. Li, C. Wang, X. Wang, and L. Bi, Sintering aids for proton-conducting oxides – A double-edged sword? A mini review, *Electrochem. Commun.*, 112 (2020), p. 106672.
[185] M.K. Hossain, M.C. Biswas, R.K. Chanda, M.H.K. Rubel, M.I. Khan, and K. Hashizume, A review on experimental and theoretical studies of perovskite barium zirconate proton conductors, *Emerg. Mater.*, 4 (2021), No. 4, p. 999.
[186] D. Han, N. Hatada, T. Uda, and R. Koc, Chemical Expansion of Yttrium-Doped Barium Zirconate and Correlation with Proton Concentration and Conductivity, *J. Am. Ceram. Soc.*, 99 (2016), No. 11, p. 3745.
[187] I. Ahmed, S. Eriksson, E. Ahlberg, C. Knee, H. Gotlind, L. Johansson, M. Karlsson, A. Matic, and L. Borjesson, Structural study and proton conductivity in Yb-doped $BaZrO_3$, *Solid State Ion.*, 178 (2007), No. 7-10, p. 515.
[188] J.L. Yin, X.W. Wang, J.H. Xu, H.T. Wang, F. Zhang, and G.L. Ma, Ionic conduction in BaCe0.85-xZrxEr0.15O3-alpha and its application to ammonia synthesis at atmospheric pressure, *Solid State Ion.*, 185 (2011), No. 1, p. 6.
[189] E. Gorbova, V. Maragou, D. Medvedev, A. Demin, and P. Tsiakaras, Investigation of the protonic conduction in Sm doped $BaCeO_3$, *J. Power Sources*, 181 (2008), No. 2, p. 207.
[190] A. Afif, N. Radenahmad, J. Zaini, M. Abdalla, S. Rahman, S. Eriksson, and A. Azad, Enhancement of proton conductivity through Yb and Zn doping in $BaCe_{0.5}Zr_{0.35}Y_{0.15}O_{3-\delta}$ electrolyte for IT-SOFCs, *Proc. Appl. Ceram.*, 12 (2018), No. 2, p. 180.
[191] R. Murphy, Y. Zhou, L. Zhang, L. Soule, W. Zhang, Y. Chen, and M. Liu, A new family of proton‐conducting electrolytes for reversible solid oxide cells: $BaHf_xCe_{0.8-x}Y_{0.1}Yb_{0.1}O_{3-\delta}$, *Adv Funct Mater*, 30 (2020), No. 35, p. 2002265.
[192] K. Leonard, J. Druce, V. Thoreton, J.A. Kilner, and H. Matsumoto, Exploring mixed proton/electron conducting air electrode materials in protonic electrolysis cell, *Solid State Ion.*, 319 (2018), p. 218.
[193] C. Duan, J. Tong, M. Shang, S. Nikodemski, M. Sanders, S. Ricote, A. Almansoori, and R. O'Hayre, Readily processed protonic ceramic fuel cells with high performance at low temperatures, *Science*, 349 (2015), No. 6254, p. 1321.
[194] E. Traversa, S.P. Shafi, E.H. Daas, and L. Bi, Tailoring the cathode-electrolyte interface with nanoparticles for boosting the solid oxide fuel cell performance of chemically stable proton-conducting electrolytes, *Small*, 14 (2018), No. 32, p. 1801231.
[195] S. Choi, T.C. Davenport, and S.M. Haile, Protonic ceramic electrochemical cells for hydrogen production and electricity generation: exceptional reversibility, stability, and demonstrated faradaic efficiency, *Energy Environ. Sci.*, 12 (2019), No. 1, p. 206.
[196] K. Wei, N. Li, Y. Wu, W. Song, X. Wang, L. Guo, M. Khan, S. Wang, F. Zhou, and Y. Ling, Characterization and optimization of highly active and Ba-deficient $BaCo_{0.4}Fe_{0.4}Zr_{0.1}Y_{0.1}O_{3-\delta}$-based cathode materials for protonic ceramics fuel cells, *Ceram. Int.*, 45 (2019), No. 15, p. 18583.
[197] H. Ding, W. Wu, C. Jiang, Y. Ding, W. Bian, B. Hu, P. Singh, C.J. Orme, L. Wang, and Y. Zhang, Self-sustainable protonic ceramic electrochemical cells using a triple conducting electrode for hydrogen and power production, *Nat. Commun.*, 11 (2020), p. 1907.
[198] N. Wang, H. Toriumi, Y. Sato, C. Tang, T. Nakamura, K. Amezawa, S. Kitano, H. Habazaki, and Y. Aoki, $La_{0.8}Sr_{0.2}Co_{1-x}Ni_xO_{3-\delta}$ as the efficient triple conductor air electrode for protonic ceramic cells, *ACS Appl. Energy Mater.*, 4 (2020), No. 1, p. 554.
[199] Y. Zhou, E. Liu, Y. Chen, Y. Liu, L. Zhang, W. Zhang, Z. Luo, N. Kane, B. Zhao, and L. Soule, An active and robust air electrode for reversible protonic ceramic electrochemical cells, *ACS Energy Lett.*, 6 (2021), No. 4, p. 1511.
[200] Y. Li, S. Wang, and P.-C. Su, Proton-conducting micro-solid oxide fuel cells with improved cathode reactions by a nanoscale thin film gadolinium-doped ceria interlayer, *Sci. Rep.*, 6 (2016), p. 22369.

[201] L.R. Tarutina, G.K. Vdovin, J.G. Lyagaeva, and D.A. Medvedev, $BaCe_{0.7-x}Zr_{0.2}Y_{0.1}Fe_xO_{3-\delta}$ derived from proton-conducting electrolytes: A way of designing chemically compatible cathodes for solid oxide fuel cells, *J. Alloys Compd.*, 831 (2020), p. 154895.

[202] Z. Wang, P. Lv, L. Yang, R. Guan, J. Jiang, F. Jin, and T. He, $Ba_{0.95}La_{0.05}Fe_{0.8}Zn_{0.2}O_{3-\delta}$ cobalt-free perovskite as a triple-conducting cathode for proton-conducting solid oxide fuel cells, *Ceram. Int.*, 46 (2020), No. 11, p. 18216.

[203] J. Liu, J. Ding, L. Miao, Z. Gong, K. Li, and W. Liu, High performance $Ba_{0.95}Ca_{0.05}Fe_{0.9-x}Sn_xY_{0.1}O_{3-\delta}$-SDC as cobalt-free cathode for intermediate-temperature proton-conducting solid oxide fuel cells with $BaZr_{0.1}Ce_{0.7}Y_{0.2}O_{3-\delta}$ electrolyte, *J. Alloys Compd.*, 786 (2019), p. 163.

[204] M. Saqib, I.-G. Choi, H. Bae, K. Park, J.-S. Shin, Y.-D. Kim, J.-I. Lee, M. Jo, Y.-C. Kim, and K.-S. Lee, Transition from perovskite to misfit-layered structure materials: a highly oxygen deficient and stable oxygen electrode catalyst, *Energy Environ. Sci.*, 14 (2021), No. 4, p. 2472.

[205] X. Zhou, N. Hou, T. Gan, L. Fan, Y. Zhang, J. Li, G. Gao, Y. Zhao, and Y. Li, Enhanced oxygen reduction reaction activity of $BaCe_{0.2}Fe_{0.8}O_{3-\delta}$ cathode for proton-conducting solid oxide fuel cells via Pr-doping, *J. Power Sources*, 495 (2021), p. 229776.

[206] Z. Zhao, J. Cui, M. Zou, S. Mu, H. Huang, Y. Meng, K. He, K.S. Brinkman, and J.J. Tong, Novel twin-perovskite nanocomposite of Ba–Ce–Fe–Co–O as a promising triple conducting cathode material for protonic ceramic fuel cells, *J. Power Sources*, 450 (2020), p. 227609.

[207] W. Li, B. Guan, T. Yang, Z. Li, W. Shi, H. Tian, L. Ma, T.L. Kalapos, and X. Liu, Layer-structured triple-conducting electrocatalyst for water-splitting in protonic ceramic electrolysis cells: Conductivities vs. activity, *J. Power Sources*, 495 (2021), p. 229764.